Title

Lung Motion Model Validation Experiments, Free-Breathing Tissue Densitometry, and Ventilation Mapping using Fast Helical CT Imaging

Author

Dou, Tai H.

Publication Date

2016

Peer reviewed|Thesis/dissertation

UNIVERSITY OF CALIFORNIA

LOS ANGELES

Lung Motion Model Validation Experiments, Free-Breathing Tissue Densitometry, and Ventilation Mapping using Fast Helical CT Imaging

A dissertation submitted in partial satisfaction of the

requirements for the degree Doctor of Philosophy

in Biomedical Physics

by

Hsiang-Tai Dou

2016

ABSTRACT OF THE DISSERTATION

Lung Motion Model Validation Experiments, Free-Breathing Tissue Densitometry and Ventilation Mapping using Fast Helical CT Imaging

by

Hsiang-Tai Dou

Doctor of Philosophy in Biomedical Physics

University of California, Los Angeles, 2016

Professor Daniel Abraham Low, Chair

The uncertainties due to respiratory motion present significant challenges to accurate characterization of cancerous tissues both in terms of imaging and treatment. Currently available clinical lung imaging techniques are subject to inferior image quality and incorrect motion estimation, with consequences that can systematically impact the downstream treatment delivery and outcome. The main objective of this thesis is the development of the techniques of fast helical computed tomography (CT) imaging and deformable image registration for the radiotherapy applications in accurate breathing motion modeling, lung tissue density modeling and ventilation imaging.

Fast helical CT scanning was performed on 64-slice CT scanner using the shortest available gantry rotation time and largest pitch value such that scanning of the thorax

region amounts to just two seconds, which is less than typical breathing cycle in humans. The scanning was conducted under free breathing condition. Any portion of the lung anatomy undergoing such scanning protocol would be irradiated for only a quarter second, effectively removing any motion induced image artifacts. .The resulting CT data were pristine volumetric images that record the lung tissue position and density in a fraction of the breathing cycle. Following our developed protocol, multiple fast helical CT scans were acquired to sample the tissue positions in different breathing states. To measure the tissue displacement, deformable image registration was performed that registers the non-reference images to the reference one.

In modeling breathing motion, external breathing surrogate signal was recorded synchronously with the CT image slices. This allowed for the tissue-specific displacement to be modeled as parametrization of the recorded breathing signal using the 5D lung motion model. To assess the accuracy of the motion model in describing tissue position change, the model was used to simulate the original high-pitch helical CT scan geometries, employed as ground truth data. Image similarity between the simulated and ground truth scans was evaluated. The model validation experiments were conducted in a patient cohort of seventeen patients to assess the model robustness and inter-patient variation. The model error averaged over multiple tracked positions from several breathing cycles was found to be on the order of one millimeter.

In modeling the density change under free breathing condition, the determinant of Jacobian matrix from the registration-derived deformation vector field yielded volume change information of the lung tissues. Correlation of the Jacobian values to the corresponding voxel Housfield units (HU) reveals that the density variation for the

majority of lung tissues can be very well described by mass conservation relationship. Different tissue types were identified and separately modeled. Large trials of validation experiments were performed. The averaged deviation between the modeled and the reference lung density was 30 HU, which was estimated to be the background CT noise level.

In characterizing the lung ventilation function, a novel method was developed to determine the extent of lung tissue volume change. Information on volume change was derived from the deformable image registration of the fast helical CT images in terms of Jacobian values with respect to a reference image. Assuming the multiple volume change measurements are independently and identically distributed, statistical formulation was derived to model ventilation distribution of each lung voxels and empirical minimum and maximum probability distribution of the Jacobian values was computed. Ventilation characteristic was evaluated as the difference of the expectation value from these extremal distributions. The resulting ventilation map was compared with an independently obtained ventilation image derived directly from the lung intensities and good correlation was found using statistical test. In addition, dynamic ventilation characterization was investigated by estimating the voxel-specific ventilation distribution. Ventilation maps were generated at different percentile levels using the tissue volume expansion metrics.

The dissertation of Hsiang-Tai Dou is approved.

Nzhde Agazaryan

Magnus Dahlbom

Reinhard Schulte

Daniel Abraham Low, Committee Chair

University of California, Los Angeles

2016

DEDICATION

To my family

and

my wife,

Yuji Liao

TABLE OF CONTENTS

† - The chapter contains material published in Medical Physics.
‡ - The chapter contains material published in International Journal of Radiation Oncology·Biology·Physics.
* - The chapter contains material being prepared for publication.

ACKNOWLEDGMENTS

I would like to express my appreciation for my advisor, Daniel Low, in guiding me through my graduate studies. I am grateful for his mentorship and engagement in my research projects. Dan is a role model for me in activism, scholarship, and leadership. I would like to thank Dan for introducing me to the field of medical physics. He has mentored me to become an independent researcher to develop research projects from conception to completion and given me freedom to explore and pursue topics of my curiosity.

I was very fortunate to be able to work with many great people both in the UCLA RadOnc and through my research collaboration. I thank Dan Ruan for her expertise and fruitful discussions that help transform our ideas into great research work. David Thomas has been generous in sharing his knowledge and experience to get me started in 4DCT projects. John Lewis for providing insightful comments. Special thanks go to Nzhde Agazaryan, Steve Tenn, and Chul Lee for the instructions and training in practical clinical knowledge. I appreciate very much the collaboration with Mattias Heinrich and our great discussions on deformable registration and its applications. In addition, I am deeply grateful to Reinhard Schulte, who has introduced me to proton therapy.

I also want to extend my thanks to the UCLA Biomedical Physics inter-departmental graduate program for providing the outstanding resources and environment for both education and research. I thank Mike McNitt-Gray and Magnus Dahlbom for their support and guidance during my time at UCLA.

Finally, I thank my family for their love and support. I am grateful for my wife, Yuji, for being my best friend through these years and the beautiful memories that we shared outside of work under the blue skies in sunny California.

CURRICULUM VITAE

Education

M.S. 2014	University of California, Los Angeles Biomedical Physics Advisor: Daniel A. Low
M.S. 2009	Ludwig-Maximilians-Universität, Munich, Germany Physics Diploma Thesis: "Towards Single Molecule Imaging in an Ion Trap" Advisor: Tobias Schaetz, Max Planck Institute for Quantum Optics
B.S. 2004	University of California, Los Angeles Physics

Awards

2014-15	UCLA Graduate Research Mentorship Program
2015-16	UCLA Dissertation Year Fellowship
2015	Norm Baily Award (AAPM Southern California Chapter)
2016	Norm Baily Award (AAPM Southern California Chapter)

Peer-Reviewed Publications

TH Dou, D Ruan, M Heinrich, and DA Low. Characterization of Lung Ventilation and Dynamic Lung Ventilation Mapping using Fast Helical CT Protocol, in preparation

TH Dou, D Ruan, M Heinrich, and DA Low. A method for characterizing and validating dynamic lung density change during quiet respiration, in preparation

TH Dou, D Thomas, D O'Connell, J Bradley, J. Lamb, and DA Low. Simulation of 4DCT Tumor Motion Measurement Errors, *Med. Phys*, **42 (10)** 6084, 2015.

TH Dou, Thomas DH, O'Connell DP, Lamb JM, Lee P, Low DA. A method for assessing ground-truth accuracy of the 5DCT technique. *International Journal of Radiation Oncology * Biology * Physics* **93 (4)** 925-933, 2015.

DP O'Connell, DH Thomas, TH Dou, JM Lamb, F Feingold, MK Fuld, JP Sieren, CM Sloan, MA Shirk, EA Hoffman, C Hofmann, DA Low. Comparison of a breathing gated CT images generated using a 5DCT technique and a commercial clinical protocol in a porcine model, *Med. Phys,* **42 (7)** 4033, 2015

DA. Low, D Morele, P Chow, TH Dou, T Ju. Does the γ dose distribution comparison technique default to the distance to agreement test in clinical dose distributions? *Med. Phys,* **40 (7)**, 071722, 2013

AP. Santhanam, Y. Min, TH Dou, P. Kupelian and D. Low. A client-server framework for 3D remote visualization of radiotherapy treatment space, *Frontiers in Oncology,* **3 (18)** 1-7**,** 2013

Dou, T.H., Tautz, R., Gu, X., Marcus, G., Feurer, T., Krausz, F. and Veisz, L., 2010. Dispersion control with reflection grisms of an ultra-broadband spectrum approaching a full octave. *Optics express*, *18*(26), pp.27900-27909.

Conference Proceeding

TH Dou, Yugang Min, John Neylon, David Thomas, Patrick Kupelian, Anand Santhanam. Fast simulated annealing and adaptive Monte Carlo sampling based parameter optimization for dense optical-flow deformable image registration of 4DCT lung anatomy, Proc. SPIE 9786, Medical Imaging 2016: Image-Guided Procedures, Robotic Interventions, and Modeling, 97860N (March 18, 2016); doi:10.1117/12.2217194.

Chapter 1

Introduction

Lung diseases, such as COPD and lung cancer, are aggressive forms of disease that claim high mortality rates. COPD, which includes chronic bronchitis and emphysema, affected more than 8 million people in the US and was ranked 3rd as cause of death of all diseases behind cancer and heart disease. Lung cancer is another form of serious lung disease that accounts for the largest fraction of cancer-related deaths both in the US and worldwide [1]. The disease often poses a serious challenge for the clinicians due to the spread of large tumor volumes in the chest, often invading critical vital organs such as the lungs, the large blood vessels, and the esophagus. Radiation therapy (RT) is a promising treatment option for lung cancer because it can be delivered noninvasively and bears curative potential. Recent advances in high-dose conformal radiation therapy have resulted in significant gains in tumor control and overall survival [2, 3].

1.1 Overview of radiation therapy

Radiation therapy is a form of cancer treatment that applies high energy radiation to locally eradicate malignant cells and has also been used in combination with surgery and chemotherapy. Depending on the tumor type, location, stage, and patient health condition, radiation may be administered with curative, adjuvant, neoadjuvant, or palliative intent. Radiation therapy accomplishes tumor control through the ionizing radiation, which generate free radicals and reactive oxygen species. These highly active agents tend to

interact with and damage the DNA molecules, leading to cell death and tumor shrinkage. Radiation therapy can be delivered using external sources, such as linear accelerator, or internal sources, such as brachytherapy.

In order to achieve the desired therapeutic effect that maximizes the radiation delivered to the tumor area while minimizing the radiation exposure to the normal healthy tissues, a general workflow has been established to simulate the realistic treatment conditions while taking into account the various treatment delivery uncertainties. The first step of this workflow involves obtaining the patient anatomy through computed tomography (CT) scanning. CT scans delineate the target area in relation to the surround organs and contain the electron density information, which is essential to the treatment planning process. In the treatment planning stage, the target and neighboring organs are first contoured, and the dose is prescribed to the target area. The planning software computes the optimal dose distribution, taking into account the dose conformality to the target region, the patient positioning uncertainties, the beam angle sequence and the priorities of normal organs to spare. In the treatment delivery phase of the workflow, the patient is carefully positioned under the treatment gantry either through stereotactic fixtures or cone beam CT image guidance, where the patient position is adjusted until it matches that from the planning session. Once the positioning is complete, the radiation beam is delivered according to the treatment plan.

Advances in intensity modulated radiation therapy have enabled conformal radiation delivery with great targeting precision. These conformal techniques facilitate target dose escalation with the aim of improving survival and normal tissue sparing. The accuracy of the conformal techniques is, however, limited by the uncertainties in patient positioning

and internal motion. Sources of internal motion can be divided into intrafraction and interfraction components. Four dimensional computed tomography (4DCT) imaging technologies have shown that significant organ motion can occur during radiation treatment [4, 5]. If left uncompensated, such motion may lead to significant dose delivery errors, as shown in many recent investigations. Sources of uncertainties may result from any of the aforementioned stages in the radiotherapy workflow. In the simulation stage, motion-induced uncertainties manifest themselves most prominently in the image artifacts, which adversely affect the dose computation accuracy. In treatment planning, the coverage of the tumor volume is limited by the accuracy in the margin definition. The spatial extent of tumor under respiratory motion is accounted for using the planning target volume (PTV). Over-estimated PTV would result in surrounding healthy tissues receiving more dose while under-estimating the motion range would result in under-irradiation of the gross tumor volume (GTV). In terms of radiation delivery, motion can lead to dose blurring around the edge of the target volume. In case of IMRT treatments, where the multileaf collimator (MLC) constantly shifts, interplay effects can also occur. Further dose error can include dose deformation effects that take place along the boundary of the tissue interface, where high density difference occurs.

1.2 Treatment strategies for mobile tumors

Various techniques have been designed to address motion-induced uncertainties during radiation therapy. These methods range from motion-inclusive margin treatment, to target immobilization, gated radiation delivery, and finally real-time radiation beam tracking the moving tumor. The following sections provide a brief survey of these techniques.

1.2.1 ITV

Respiratory motion increases the apparent size of the tumor and necessitates larger aperture size. Traditionally, a safety margin is added to the CTV to create the planning target volume (PTV). The larger treatment margin leads to the irradiation of normal lung tissues. The size of the margin has to be chosen carefully; it should be large enough to ensure the delivery of the prescribed dose to a moving target and small enough to keep the normal tissue complications to an acceptable level. In the following, we review a number of strategies for treatment delivery under free breathing condition.

Accounting for tumor motion is crucial in patients undergoing radiation therapy under free-breathing condition. Tumor motion amplitude depends on its anatomical location and can be large towards the diaphragm. To account for the uncertainties in the size, shape and position of the clinical target volume, the International Commission on Radiation Units and Measurements has devised the concept of an internal target volume (ITV) to provide an envelope for target motion in Report 83 [6]. More specifically, ITV was defined to encompass the geometrical locations of the GTV in all of the breathing phases. The delineation of the ITV can be performed through manual or automatic contouring of the GTV in each phase of the 4DCT image set. Alternative method was proposed that creates an image of maximal intensity projection through combining the set of 4DCT images from the whole breathing cycle [7-9]. Such approach was found to be equivalent to the composite contour generated from the individual breathing phases [10].

ITV delineation is subject to the risks of both geographic miss and irradiation of healthy tissues. Multiple studies have investigated the uncertainties in ITV quantification due to

different imaging and post-processing techniques [11-13]. In [9], the authors reported that the median and range of the ITV for 20 stage I SBRT patients were 7.6 (1.1–35.6), 10.2 (1.9–43.7), and 9.0 (1.3–37.3) cm^3 from helical-, MIP-, and average intensity define ITV. These studies found that MIP-based ITV can most effectively capture the tumor excursion [9, 14]. However, caution needs to be exercised as commercial clinical 4DCT imaging might not capture the full extent of tumor motion since the axial scanning in CT imaging takes much longer than the breathing cycle and each image slice contains breathing information only from one or two breathing cycles. ITV generation using CBCT imaging has been investigated in [15]. Adopting PET defined dynamic tumor volume was explored in [16].

1.2.2 Breath hold

Controlling tumor motion can potentially remove the motion uncertainty, which was observed to be larger than setup uncertainties [17]. Moreover, lung tissues are susceptible to late radiation response, such as pneumotitis and fibrosis [18] and these effects are related to the irradiated lung volume [19, 20]. In [21-23], the authors at MSKCC presented deep inhalation breath hold (DIBH) technique where the patients were coached into deep inspiration and breath holding, with the lung inflation level monitored by spirometer and the diaphragm position recorded by fluroscopy. The DIBH technique was motivated by the benefits of decreased lung density and the potential for treatment margin reduction, both of which facilitate target dose escalation and normal tissue sparing. In the 5 patients of this study, the range of comfortable breath hold duration was reported to be 12-16 s. The average centroid position of the GTV was found to be 0.2±1.4 mm for diaphragm

displacements of -1.0±4.0 mm from CT scans. Barnes et al [24] showed a significant reduction in the percent lung volume receiving ≥ 20 Gy at DIBH compared to free breathing condition. Disadvantages to the DIBH technique include patient intolerability of the maneuver and poor reproducibility due to residual tumor movement.

1.2.3 Beam gating

Gated radiation delivery aims at target motion reduction during irradiation. A radiation beam gating methodology was first presented by Ohara et al [25], where the signal from an implanted gold marker was used to control the linear accelerator in real time. Respiration gate was also employed at the Proton Research Medical Center of the Tsukuba University in Japan, where a strain gauge detector was used to trigger the proton accelerator [26]. Later, at the University of California, Davis, signals from video camera were used to switch the radiation beam on and off [27, 28]. The respiratory gating device has since been made commercially available as the real-time position management respiratory gating system (RPM), for which clinical studies can be found in [29, 30]. Compared to breath hold techniques, gated treatments require less patient effort.

When considering employing breathing gating, the gating window was typically selected to be near the full exhalation phase, which reflects the most reproducible portion of the breathing cycle. For respiratory gated radiotherapy, the internal margin is determined using the target displacement within the gating window (e.g. 50% phase ± 10%). Gating can be performed using specific amplitude level of the breathing signal and the pre-defined gating window. It was found that tumor motion correlated well with external fiducial marker in the thorax and abdomen [31, 32]. In spite of generally good external-to-internal

correlation, large residual tumor motion can occur relative to the measured surrogate signal [31, 32]. In addition, in gating for an irregular breathing patient, phase gating is susceptible to larger residual error due to significant cycle-to-cycle variability or slow drift in target position or breathing signal. To improve treatment efficiency, more robust gating techniques have been proposed, including the hybrid gating method involving high frequency external surrogate sampling and intermittent internal marker update [33], and markerless template matching techniques using fluoroscopic imaging [34-37] In addition, irregular breathing pattern compromises gated treatment accuracy, as was found in a simulation study comparing phase-binned 4DCT and dynamic MRI images by Cai et al [38]. The problems in gated radiation therapy lead to the development of treatment delivery systems that integrate real time imaging devices.

1.2.4 Beam tracking

The next level of target motion compensation can be performed by synchronizing the radiation beam to the motion of the target. Such technique affords therapeutic benefit of margin reduction similar to beam gating methods, but with continuous irradiation it can do so without prolonging the treatment time. Beam tracking was first proposed by Keall et al for motion adaptive photon therapy [39]. As a commercial solution, a dynamic tracking technique has been implemented in Cyberknife Synchrony [40], where the correlation between the LED markers placed on the patient chest wall and internal tumor position (based on the position of implanted markers) is used to construct a correspondence model. During the therapy session, the LED markers monitor the patient breathing, and the signal is fed into the correspondence model for predicting the tumor position. The tumor position

prediction is verified from time to time using x-ray imaging. The Synchrony technology builds into the possibility of updating the correspondence model or completely re-construct the correspondence model.

The ultimate goal of image-guided radiation therapy is the capability of tracking target motion in real-time. Compared to existing tumor tracking techniques, magnetic resonance imaging (MRI) features ionization-radiation-free imaging and superior soft tissue contrast compared to CT modalities such that its integration into the radiation treatment machine allows for real-time visualization of the organ movement during treatment. In addition, similar to CBCT, pre-treatment MR imaging also holds the potential to improve patient positioning accuracy. Such MRI-guided radiation delivery devices have been proposed for a $Cobalt^{60}$ source [41] and linear accelerator [42, 43] delivery systems. The integration of dynamic real time MLC unit into the MRI-guided radiation delivery would enable ideal target dosimetric conformality.

1.3 Four dimensional computed tomography

In the last decade, 4DCT or respiration-correlated CT has become the indispensable clinical tool that provides patient breathing model for radiation therapy. 4DCT provides the 3D anatomical information for each phase in the respiratory cycle, from which patient breathing pattern and tumor motion range can be extracted.

Treatment planning for respiratory gated radiotherapy was motivated by the cardiac gating on diagnostic CT scanners. Modern 4DCT techniques were launched following the works by Vedam et al [44] and Ford et al [45]. The implementation of these techniques

assumes the periodicity of patient breathing pattern and assigns the continuously acquired images to the pre-defined breathing phases, which are measured quantities from external surrogates. Low et al [46] proposed an alternative 4DCT technique that acquires images in cine mode with the simultaneous recording of the patient spirometry. Such tidal volume based retrospective sorting method allows for a more patient physiological approach to 4DCT imaging.

1.3.1 Model-based 4DCT

Volumetric images of the lung anatomy in time series may yield biomechanical information of the thorax region in addition to the position and density of the lung tissues. One the early works in this area was performed by McClelland et al., where an average respiratory cycle was constructed and a B-spline fitting was employed to generate a continuous 4D motion model [47]. To our knowledge, there are two approaches to modeling the spatiotemporal motion that do not assume periodicity in breathing pattern. Recently, principal component analysis (PCA) based approaches have also been proposed [48, 49]. The PCA was used to analyze the underlying data structure of the deformation vector fields obtained from deformable image registration processing of the 4DCT image data between a reference phase and other phases. The authors found that three principal components were sufficient to describe the respiratory motion based on 4DCT data, with the first principal component basis characterizing the regular respiratory motion, while the rest of the bases account for the variation caused by image noise, registration error, or image reconstruction errors. The second modeling approach is due to Low et al., which formulates the tissue displacement as a linear model of the measured tidal volume and

airflow using spirometry [50]. This modeling approach is motivated by breathing physiological measurement and allows for the characterization of irregular breathing pattern and tissue hysteresis trajectory. Zhao et al tested the model performance in a large group of patients [51].

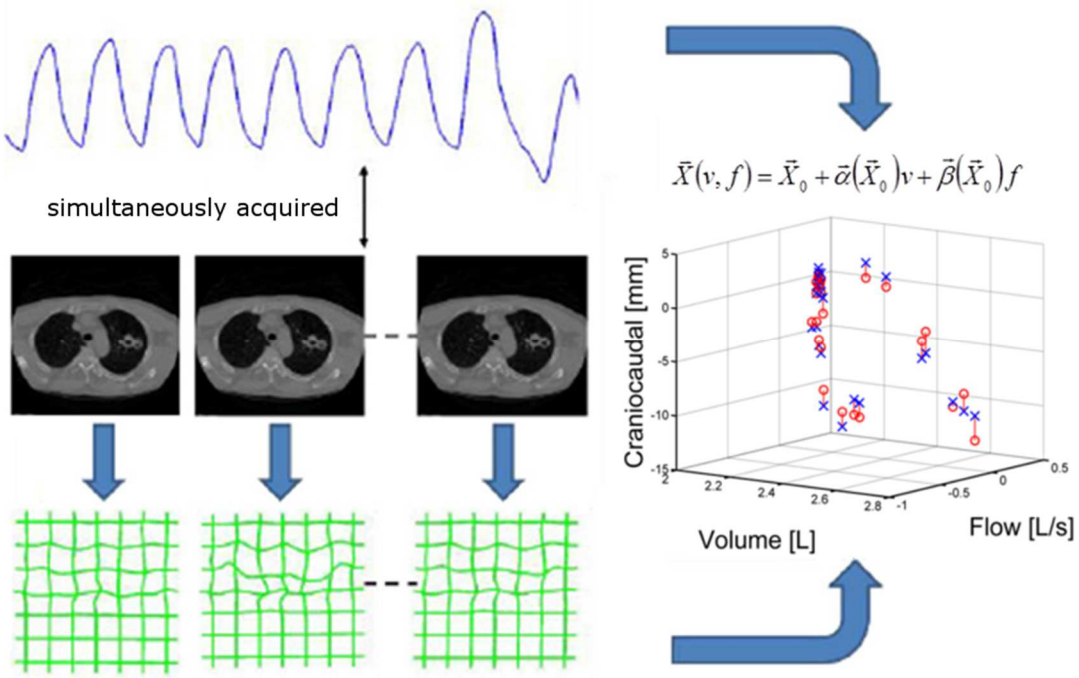

Figure 1. A schematic for constructing a breathing motion model that incorporates external surrogate measurement, internal image acquisition, and motion measurement using deformable image registration together into a motion model that correlates the between the external and internal breathing data.

1.3.2 Lung ventilation imaging

Radiation can induce tissue material changes in the lung parenchyma and alter respiratory mechanics. This damage can be significant in lung cancer patients with marginal lung function and may lead to symptomatic pulmonary dysfunction [52]. Volumetric functional lung imaging provides a clinical tool to assess the pulmonary function distribution and

optimize radiation treatment planning to avoid regions of high physiological importance. A variety of imaging modalities has been employed for lung functional imaging. Positron emission tomography and single photon emission CT (SPECT) have been introduced clinically for assessing the lung function, but are limited by their low spatial resolution [53]. Hyperpolarized helium-3 magnetic resonance imaging has been developed for lung ventilation imaging [54-56]. While it presents the advantage of no radiation exposure, it is too costly for widespread clinical use. Xe-enhanced CT (Xe-CT) measures regional ventilation by comparing the gas wash-in and wash-out rates on the CT images [57]. Recently, 4DCT respiratory gated imaging together with image processing techniques have allowed for ventilation estimation [58].

1.4 Organization and Objectives

The dissertation is organized into the following chapters.

Chapter 2 discusses the current problems in clinical 4DCT imaging protocol. A simulation of the 4DCT scanning process was performed using a large set of patient data. The accuracy of the tumor motion estimation was evaluated using the alternative 5DCT protocol as reference.

Chapter 3 offers the background information of the framework for performing patient imaging and analysis in the subsequent chapters. The fast helical CT protocol for patient imaging and deformable image registration for processing the patient image data are presented here.

Chapter 4 discusses the validation experiments conducted on the patient cohort that underwent the 5DCT protocol. The reconstructed patient free-breathing images were compared against the fast helically acquired CT images, which were taken as ground truths.

Chapter 5 describes the lung tissue density modeling that was constructed from the fast helical CT image data acquired under free breathing condition. We show that the correlation of the CT Hounsfield value change to the determinant of the Jacobian can be used to characterize the lung tissue density change in quiet breathing.

Chapter 6 gives the account of how ventilation mapping can be obtained using fast helical CT protocol. We show that the range of the Jacobian values of each piece of lung tissue indicate how well the gas exchange takes place. In addition, a comparison study is conducted to evaluate the difference in ventilation patterns between the fast helical CT protocol and the commercial clinical 4DCT images.

Chapter 7 summarizes this dissertation work and provides an outlook for future research directions.

Chapter 2

Problems in 4DCT

Internal target motion can cause large uncertainties in radiation delivery. It has been reported that ~40% of lung tumors have displacement greater than 5 mm and 10-12% of the tumors have displacement greater than 1cm [59, 60]. To resolve the temporal changes in patient anatomy, 4DCT imaging has been clinically employed to provide spatio-temporal consistent image data. Due to the limitations in CT detector coverage and rotation time, the duration of volumetric imaging is typically larger than patient breathing cycle. Clinical 4DCT imaging solutions involve the over-sampling of the breathing data at each couch position followed by subsequent sorting process that assigns the projection images to the pre-defined time intervals of the breathing cycle. It is generally known that tumor motion variability depends on its size, shape, and position. These variations may lead to risks of tumor motion being incorrectly characterized. This chapter investigates the motion estimation by way of realistic CT scanning simulation according to clinical 4DCT scanning protocol.

2.1 Introduction

4DCT has been proposed to characterize the patient anatomical changes due to breathing motion [44-46]. The integration of 4DCT into treatment planning has the potential of reducing tumor position uncertainties due to respiratory motion so that the treatment condition can be simulated as realistically as possible. Inaccurate estimation of breathing

motion by 4DCT, however, can yield systematic errors in motion margins and inappropriate selection of motion mitigation strategies.

The generation of 4DCT images usually involves the simultaneous imaging of the anatomical site and the recording of an external surrogate signal. Analysis of the images or CT projections and the breathing cycle is used to generating CT images at pre-defined breathing phases. Commercial 4DCT techniques employ either ciné or low-pitch helical acquisition, with image reconstruction based on phase binning [44, 45, 61, 62] or amplitude binning [46, 50, 63, 64] methods. In the literature, amplitude binning approaches have been shown to be superior in reducing image artifacts than phase binning methods [64-68], but are susceptible to insufficient image data at some couch positions if respiratory cycle was missing desired amplitude due to irregular breathing. In spite of these issues, both amplitude and phase-based 4DCT protocols are still employed in the commercially available 4DCT software.

Conventional 4DCT protocols are sensitive to irregular breathing. Breathing patterns depend on the mental and physiological condition of the subject during the scanning session, and large variability is often observed. 4DCT image acquisition by low-pitch helical CT protocol can lead to motion underestimation due to, e.g. breath pauses or overestimation if the subject takes abrupt deep breaths while the tumor is being scanned. The image binning process can lead to streaking artifacts, missing image slices, and distorted shapes and volume measurements [65, 69]. The limitations of 4DCT pertaining to tumor volume definition have been investigated using internal or external breathing surrogates, where significant deviation of ciné-mode 4DCT (>50%) from realistic tumor motion was reported [11, 70, 71].

Various techniques have been proposed for retrospective sorting-based approaches with the aim of reducing irregular breathing artifacts in 4DCT images [47, 72-75]. In particular, Thomas *et al* demonstrated the acquisition of sorting-artifact-free CT images at arbitrary user-selected breathing phases based on a lung motion model [75] first published by Low *et al* [50]. This approach is termed 5DCT (three spatial dimensions along with the breathing amplitude and breathing rate). The 5DCT image acquisition aims at capturing the extent of lung tissue motion by performing multiple high-pitch (1.2) helical scans with a simultaneously recorded surrogate signal. The tissue specific displacement is obtained through deformable image registration and correlated with the measured surrogate signal such that lung tissue positions can be computed at any given breathing signal. The accuracy of the 5DCT technique has been found to be on the order of 2 mm.

In this paper, we investigate the variability of tumor motion measurements by low-pitch helical 4DCT, in which the CT scanner is run at pitches of approximately 0.06 and 0.1, selected to reflect commercial systems, such that it continuously images the mobile anatomy. A simulation was developed to determine the protocol-measured tumor motion employing actual breathing traces from 50 patients. The simulated tumor motion was compared against a percentile-based motion magnitude. Such an approach is consistent with the 5DCT technique, where the motion is characterized as a function of breathing amplitude and breathing rate. The differences between the simulated and percentile motion were used to characterize motion measurement errors due to irregular breathing.

2.2 Methods

A group of 50 patients were recruited in an IRB-approved clinical study; 26 with lung cancers and 24 with abdominal cancers. Research 5DCT scans were conducted with the patient free breathing. For this work, only the breathing traces were employed. The patient's breathing trace amplitudes were measured using a pneumatic belt (bellows). The bellows was wrapped around the patient's abdomen and as the patient inhaled and exhaled, the bellows was stretched and relaxed, causing the air pressure in the bellows to decrease and increase, respectively. A pressure transducer measured the internal air pressure and this was recorded as the breathing surrogate. This signal had been previously shown to be linearly related to the tidal volume [76]. The breathing traces were at least 5 minutes long, sampled at 100 Hz, and included normal breathing irregularities. The breathing traces had been previously corrected for baseline drift and converted to tidal volume.

A simulation was performed to determine the measured tumor motion amplitude based on the breathing trace as though the patient had been scanned using a commercial low-pitch helical protocol. For the 4DCT simulation, the scanner parameters were taken from the 16-slice Philips Big Bore 4DCT protocol: pitch of 0.06, rotation time of 0.5 second, and detector width of 2.4 centimeter and the Siemens Somatom Sensation Open that employed the same rotation time and detector width but a pitch of 0.1. This translated to irradiation times of approximately 8.3 seconds and 0.5s for stationary tissues using the 0.06 and 0.1 pitches, respectively. The images were assumed to be reconstructed using 1.5 mm thick slices.

The 4DCT approach was simulated by subdividing the craniocaudal imaging space into 1.5 mm thick slices (Figure 1). The scanner was first positioned at one end of the imaging space and its position identified at subsequent times according to its velocity and the time.

The tumor was positioned sufficiently away from the end of the imaging space so that the tumor was always in the field of view. Its position was determined by converting the breathing amplitude waveform to a tumor location. The image space slices corresponding to the tumor size and position were identified and if they overlapped the CT scanner position, those slices were identified as having imaged the tumor.

The time-sequence of the simulation was started at a selected point in the breathing cycle. Each subsequent simulation was repeated with the subsequent time bin in the breathing cycle. The breathing waveform was in the form of the digitized bellows air pressure and this needed to be converted to the cranio-caudal motion of the tumor. To accomplish this conversion, we made two assumptions. First, we assumed that the tumor motion in this dimension was linearly proportional to the breathing amplitude. This motion linearity assumption has been previously tested and reported in literature [5, 50, 77]. Further, the 90^{th} percentile (95^{th} minus the 5^{th}) of the breathing amplitude waveform was employed as the definition of the nominal breathing depth. Our percentile-based approach of inhalation/exhalation definition explicitly accounted for the relative frequencies these tidal breathing amplitudes occurred and had the additional advantage that breathing statistics were less susceptible to the influences of the few extreme shallow or deep breaths [51, 64]. The breathing waveform was converted to tumor motion by multiplying the waveform by the ratio of the nominal tumor motion (e.g. 1 cm) to the 90^{th} percentile waveform amplitude. This provided a tumor motion distribution such that the 90^{th} percentile of motion was equal to the nominal tumor motion.

The tumor was moved along the imaging space according to the scaled breathing amplitude. Overlap between the tumor and the CT slices was identified as having imaged

the tumor in that location and registered in a binary fashion. The effect of partial overlap was expected to be small and average out over the repeated simulations and did not affect the resulting

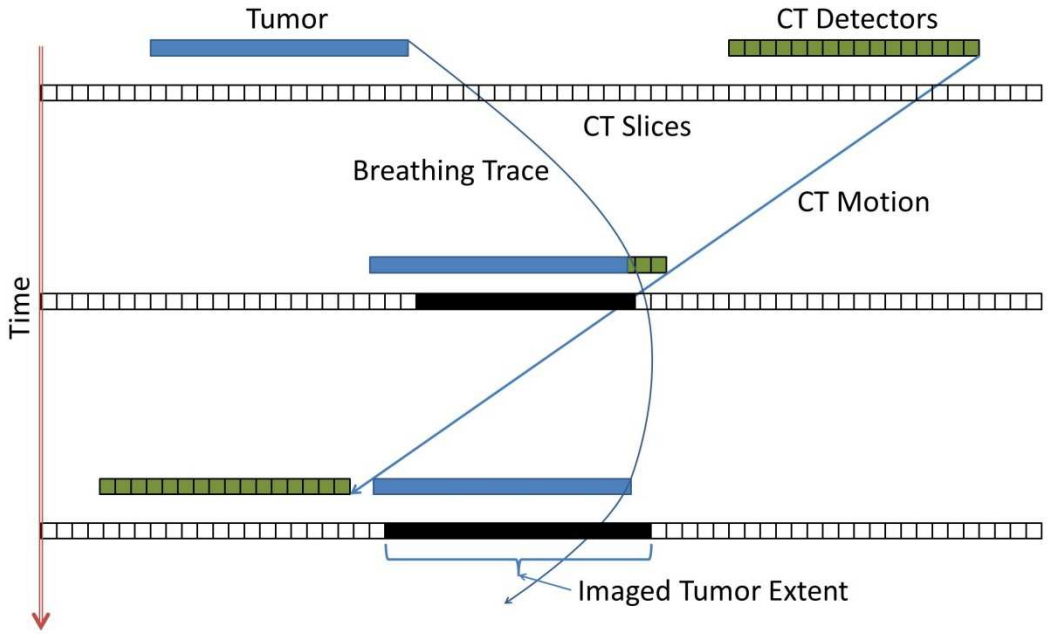

Figure 1: Schematic of 4D CT simulation model. The CT detectors move from right to left while the tumor moves along its path a distance proportional to the breathing amplitude. The CT slices are set to 0 until the tumor overlaps the moving CT detectors. For each time point, corresponding to the motion of the CT by one CT slice, the overlap is assessed and overlapping slices are set to 1. When the simulation is completed, the total of the tumor size and breathing induced motion is the extent of the imaged tumor. This process is repeated starting at sequential time points 0.1 s apart to build the statistical evaluation of the imaged tumor extent as a function of patient, tumor size, and nominal tumor motion extent.

estimated tumor motion variation. The time sequence was moved forward until the CT scanner had well passed the tumor positions. The combined overlap envelope was assumed to be an amplitude-sorted measure of the total of the tumor motion and size, so the tumor size was subtracted from the total envelope to extract the measured tumor motion. To study the clinically commonly observable tumor dimension and motion range, the process was

repeated for different combinations of nominal tumor motions of 1 cm to 4 cm in 1 cm increments and for tumor sizes of 1 cm to 4 cm in 1 cm increments.

For each patient, there was a distribution of measured motion errors for each tumor size and motion magnitude. Since the typically one-time tumor motion measurement of any 4DCT would be employed to develop a motion strategy, we treated the measured motion errors as systematic errors. Therefore, we elected to examine the greatest over- and underestimations of tumor motion by selecting the 5% of outlying cases for each of over- and underestimations. The selection of the outlier distribution was intended to reflect the scenarios where the treatment planning performed under such conditions (i.e. with a total of a 10% chance of occurring) would be conducted with an erroneous motion measurement without feedback to the clinic that this had occurred. This simulation was implemented and analyzed using MATLAB software (Mathworks, Natwick, MA).

2.3 Results

Figure 2 shows histograms of the mean of the estimated tumor motion errors and the associated standard deviation as well as the means of the 5% over- and 5% underestimated motion errors for each of the 50 patients for the 2 cm tumor size and 2 cm tumor motion simulation performed using the pitch of 0.06. The value of 100% corresponds to the 90^{th} percentile breathing amplitude, consistent with the 5DCT approach. The simulated motion estimation is compared to the 5DCT motion measurement and the estimation error is expressed as percent deviation from the 5DCT approach. Similar results were observed for the other tumor motion magnitudes and tumor sizes.

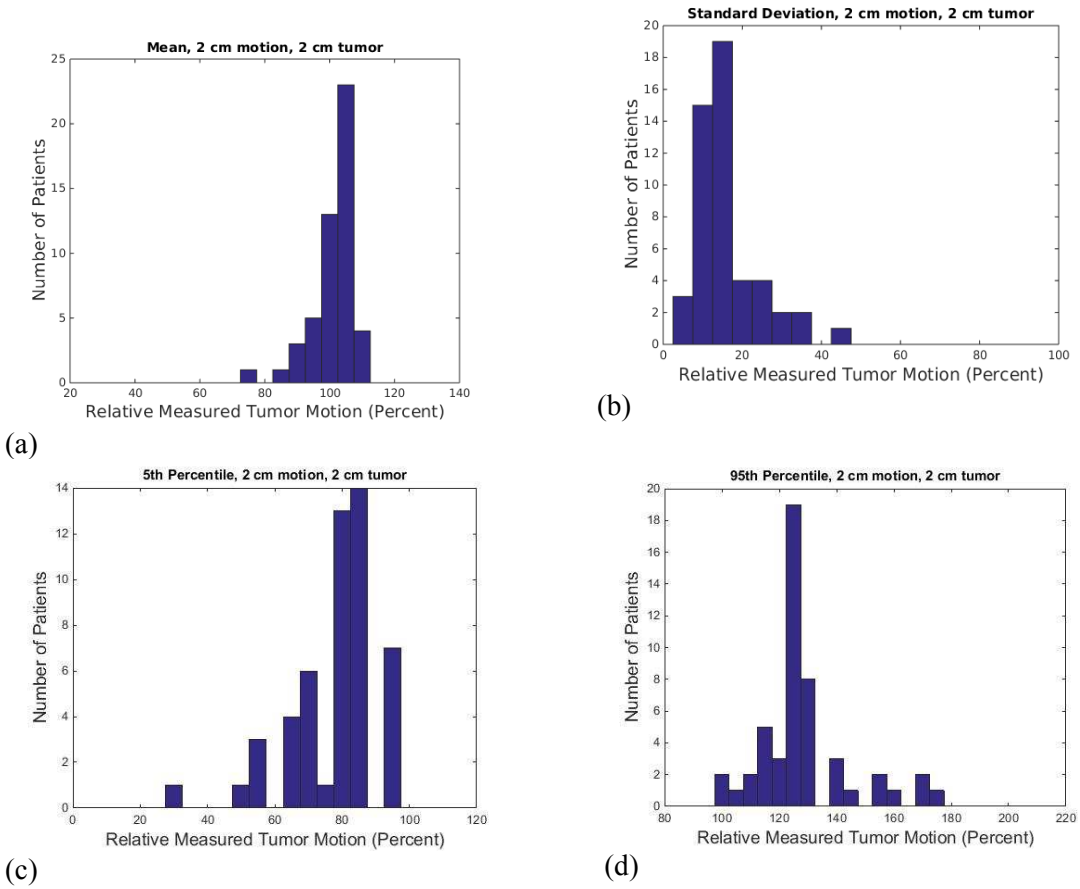

Figure 2: (a) Mean relative breathing amplitude ratio, (b) standard deviation of relative breathing amplitude ratio, (c) mean relative breathing amplitude ratio for measured motion less than the 5th percentile and (d) mean relative breathing amplitude ratio for measured motion greater than the 95th percentile. These examples are simulated for the 2 cm tumor and 2 cm nominal tumor motion magnitude f with a pitch value of 0.06.

Many of the 50 patients breathed quite regularly, so their relative motion measurements were close to 100%. This is observed both in the distribution of the mean tumor motion estimation (Fig. 2a) and their small uncertainty values (Fig. 2b) as well as in the outlier distributions (Fig 2c and 2d). On the other hand, the maximum and minimum 5% motion error ratio distributions, showed that 30% of the patients would have had breathing amplitude underestimation of at least 36% while 30% would have had overestimations of over 47%. The 16 trials (4 tumor sizes and 4 tumor motion magnitudes) provided essentially identical results due to the fact that the tumor size was subtracted from the

overall motion envelope and the motion error was evaluated as the ratio of the subsequent motion to the nominal motion magnitude.

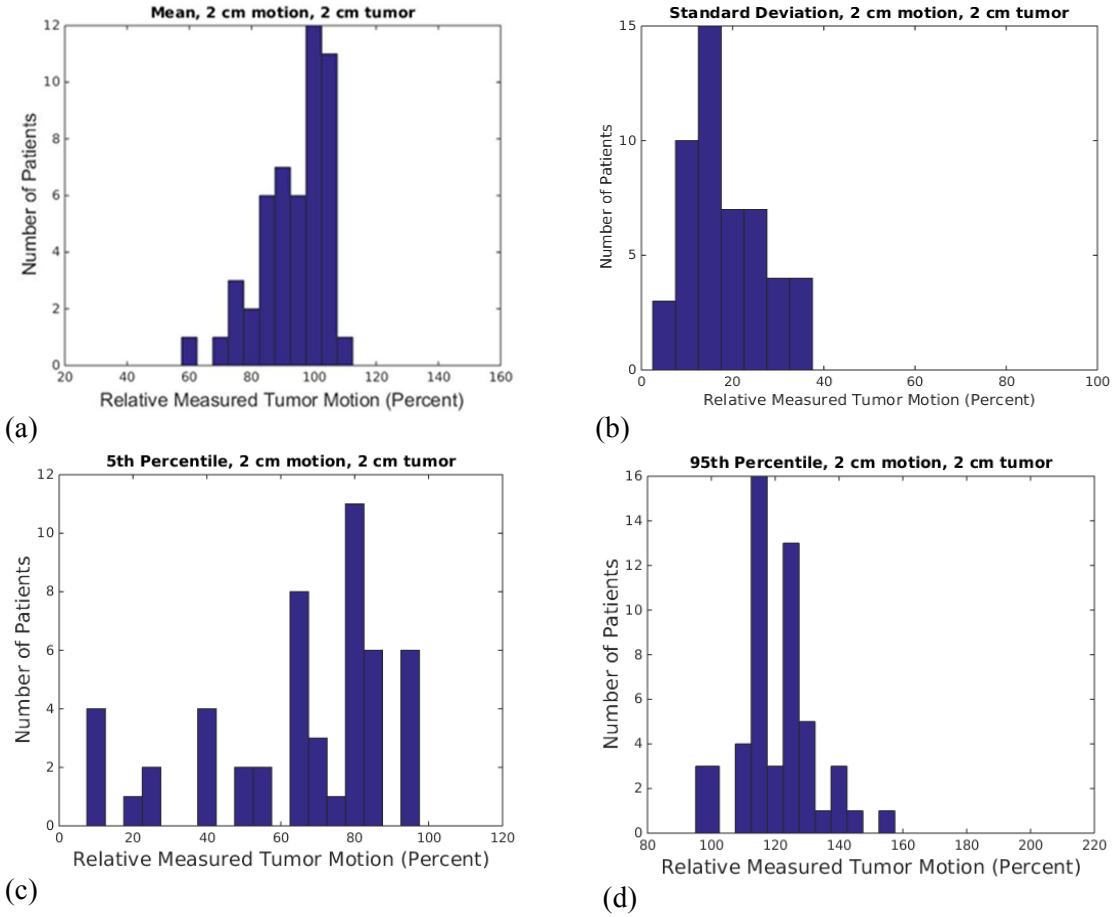

Figure 3: (a) Mean relative breathing amplitude ratio, (b) standard deviation of relative breathing amplitude ratio, (c) mean relative breathing amplitude ratio for measured motion less than the 5th percentile and (d) mean relative breathing amplitude ratio for measured motion greater than the 95th percentile. These examples are simulated for the 2 cm tumor and 2 cm nominal tumor motion magnitude using a pitch of 0.1.

Figure 3 showed the example breathing motion estimation simulated using a pitch of 0.1. Compared with the results using the pitch of 0.06, over-estimation of the imaged tumor motion decreased. On the other hand, the distribution of under-estimated tumor motion showed more deviation from the true motion amplitude. Table 1 a. and b. show the mean 5th tumor motion amplitude of the bottom 30% of the patients by the simulated tumor size

and tumor motion for the 0.06 and 0.1 pitch values, respectively. Similarly, table 1 c. and d. show the mean 95th tumor motion amplitude of the top 30% of the examined patients.

Table 1a. Mean 5th percentile amplitude of the lowest 30% relative to tumor motion in percentage for a pitch of 0.06.

size\motion (cm)\(cm)	1	2	3	4
1	70.94	62.56	61.64	61.77
2	68.06	62.36	62.32	61.88
3	66.86	64.16	61.61	61.84
4	70.58	62.72	62.52	61.13

Table 1b. Mean 5th percentile amplitude of the lowest 30% relative to tumor motion in percentage for a pitch of 0.1.

size\motion (cm)\(cm)	1	2	3	4
1	44.98	37.46	38.48	41.47
2	37.06	33.26	37.76	42.89
3	33.98	34.30	39.67	42.30
4	38.11	35.53	38.88	41.03

Table 1c. Mean 95th percentile amplitude of the upper 30% relative to tumor motion in percentage for a pitch of 0.06.

size\motion (cm)\(cm)	1	2	3	4
1	151.70	147.68	146.51	147.26
2	154.47	147.35	146.76	147.63
3	174.07	147.92	147.19	147.18
4	154.24	148.03	146.43	145.95

Table 1d. Mean 95th percentile amplitude of the upper 30% relative to tumor motion in percentage for a pitch of 0.1.

size\motion (cm)\(cm)	1	2	3	4
1	140.50	132.75	133.13	134.89
2	138.76	133.84	134.45	136.01
3	140.64	134.38	135.71	137.31
4	145.07	136.38	136.41	137.50

2.4 Discussion and Conclusion

Respiratory-gated 4DCT is an indispensable tool for characterizing breathing motion for the thorax and upper abdomen. The breathing pattern of diseased patients is often irregular. Commercial 4DCT techniques are susceptible to irregular breathing patterns, which lead to errors in treatment planning and delivery. Since 4DCT is typically performed once per patient, any resulting error can cause systematic treatment planning errors. This

work simulated the performance of low-pitch helical 4DCT acquisition in a group of 50 patients. In the examined 50-patient motion error distributions, the mean values of the fringe sub-distributions of the largest and smallest 5% of the relative motion errors were computed. For the examined patient cohort, in the worst-case scenario, the breathing amplitude was underestimated by as much as 74%, and overestimated by 177%. Our analysis using two different scanning pitch parameters showed stronger underestimation across all combinations of simulated tumor size and motion when scanned at a higher pitch of 0.1 compared to 0.06, while the opposite was true for overestimations. Explicit management of irregular breathing such as is done with the 5DCT protocol has the potential for reducing the uncertainty of the relationship between the imaged and actual tumor motions.

The present study investigated the 4DCT tumor motion measurement variability using a surrogate signal. The one dimensional analysis in the superior-inferior direction was motivated by the nearly linear relationship between the breathing amplitude and the lung tissue displacement, which has been established in literature [50, 78, 79]. Given that lung tissue motion tended to be largest in the superior-inferior dimension, the results were likely to be similar to the analysis of the 3D motion. Our simulation technique provided the advantage that many 4DCT sessions could be simulated, as opposed to image-based assessments where 4DCT data is typically a single set or a limited few. The statistics obtained from our simulations provided insight to the variability of measured tumor motion using commercial helically-based 4DCT techniques.

The technique did not consider motion hysteresis, which affects some tumors. Breathing irregularities for these tumors would be more challenging to model. The technique also

used only single breathing traces for each patient, so intra-patient variability over multiple sessions was not evaluated.

Selection of the 95th and 5th percentile breathing surrogate amplitudes to normalize the motion was arbitrary. There are no accepted definitions of inhalation and exhalation based on percentiles, but given that the results were nearly independent of tumor motion magnitude, selection of other percentiles to define the relationship between breathing magnitude and tumor motion would have provided similar results. The choice of evaluating the outlying five percent error distributions only served to show the magnitude of error in 4DCT motion estimation. Smaller outlying distributions can exhibit even larger errors, while a choice of greater percentiles would show smaller errors. We conclude that commercial clinical 4DCT images should be used with caution for patients with highly irregular breathing patterns.

Chapter 3

Framework for Experimental Data Acquisition and Analysis

4DCT imaging is an important lung imaging modality that can provide time-resolved information on both the lung anatomy and function. However, in current clinical protocols, 4DCT images may not accurately reflect the patient anatomy and motion characteristics. The former is caused by the image sorting artifacts that appear frequently as spatial inconsistencies in the acquired breathing phase specific images. The latter issue is related to the limitations in the sampling of patient breathing. Typically, breathing data of a single breath was incorporated in the 4DCT image data as the patient thoracic anatomy is imaged along the cranio-caudal axis. However, breathing variations that occur in the course of normal breathing are not taken into account. This chapter presents the novel image acquisition technique aimed at addressing these insufficiencies in conventional 4DCT imaging as well as the image processing techniques for measuring lung motion.

3.1 Fast Helical CT Protocol

To address the problems in clinical 4DCT imaging, we have proposed a novel CT imaging protocol. The core idea of our proposed image acquisition technique is to capture quasi-breath hold images from multiple breaths during patient normal breathing. The acquired set of volume images constitutes multiple samples of the lung tissues undergoing breathing

motion and allows us to determine the extent of tissue displacement. Subsequently, the tissue motion information will serve as input into a breathing motion model that would parametrize the tissue motion and render it in a continuous representation of the thoracic anatomy undergoing respiratory motion.

All patients were scanned using 64-slice CT scanners (Somatom Definition Flash and Biograph TruePoint PET·CT, Siemens Healthcare, Forchheim, Germany). Images were acquired with a nominal beam collimation (longitudinal field of view) of 64 × 0.6 mm (3.84 cm), a pitch of 1.2 and scanner rotation period of 0.285 second, which amounts to a table movement of 46.08 mm per rotation and a table velocity of 161.7 mm/s. Further scanning

Figure 1. CT scanner and breathing signal acquisition system.

parameter of 120 kV and 40 effective mAs per slice were used, which result in 169 mA for this pitch and rotation time. Images were reconstructed in slice thickness of 1-mm, using the standard Siemens reconstruction kernel B30f. Using this technique, the time to scan the entire lungs from apices to bases took approximately 2.5 seconds. In order to adequately sample the breathing motion, the complete protocol involved imaging the patient with 25 individual series (25 separate acquisitions), using alternating scanning directions with approximately 2-second delay between acquisitions. The entire scanning sequence took approximately 140 seconds. The total computed tomography dose index volume (CTDI vol) for the entire scan (all 25 acquisitions) was 4.22 cGy, which is less than a current clinical slow-helical 4D-CT protocol (Siemens Sensation Open, 800mAs, spiral pitch of 0.1, CTDI vol of 6.9 cGy). All patients imaged under this protocol were approved by the institutional review board.

3.2 Breathing Surrogate Measurement

Detailed dynamic information of the lungs can be difficult to obtain through imaging due to limitations in medical imaging. For such purposes, breathing surrogates are used to estimate the breathing state of the lungs. Breathing surrogate measurement come in a variety of forms, including but not limited to, infrared marker, spirometry, and abdominal belts. In our study, we have elected to use the abdominal pressure belt since it is less prone to the noise fluctuations in the breathing signals.

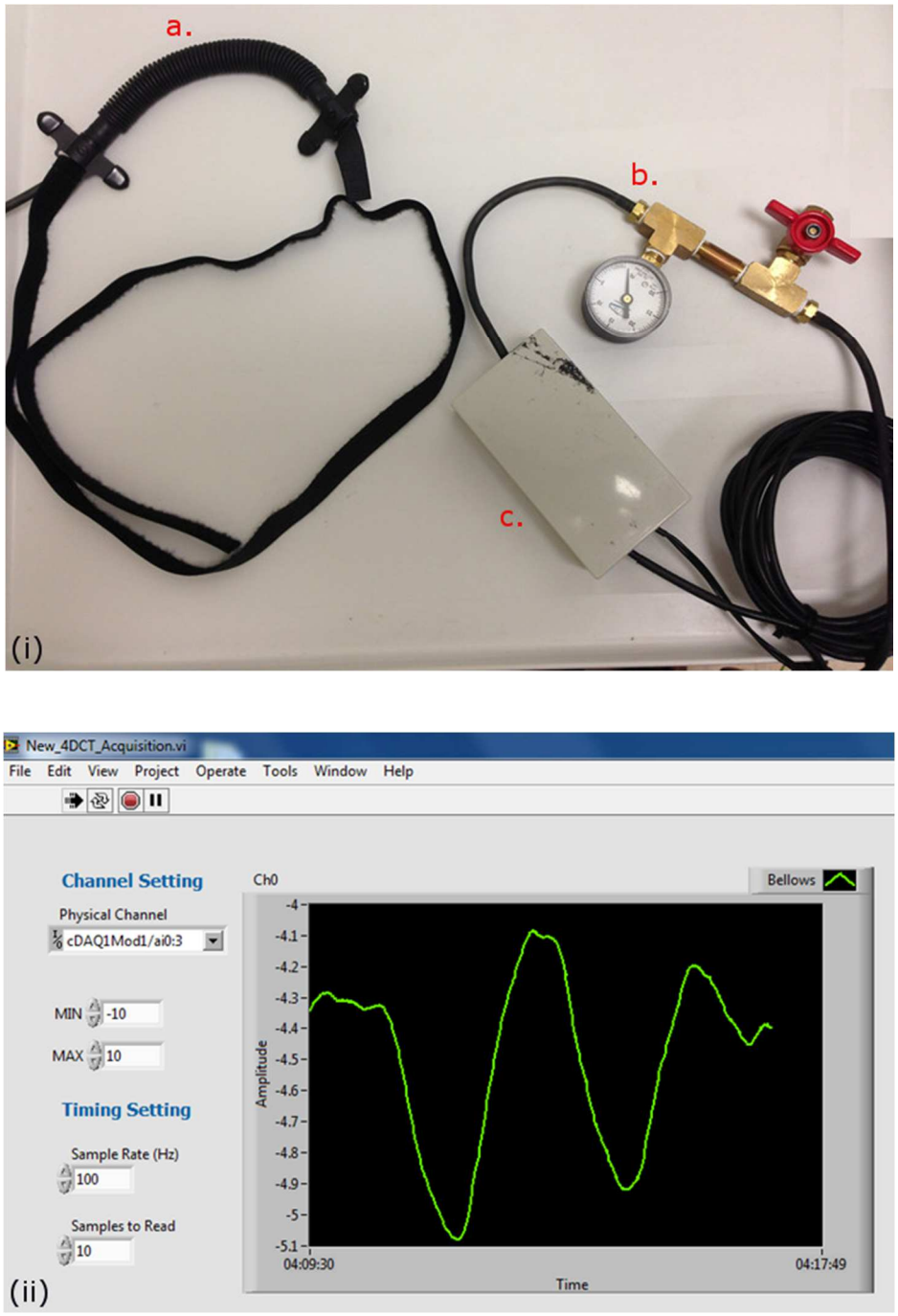

Figure 2. (i) The surrogate signal measurement system used for acquiring the breathing signal, showing, in the order of signal processing, a. the abdominal belt, b. the pressure gauge for monitoring or calibrating the pressure, and c) the pressure transducer that converts the pressure signal into electrical voltage signal. The voltage signal out of the pressure transducer is connected downstream to the data synchronization system. (ii) In-house LabVIEW Software interface for acquiring patient breathing signal.

The patient's breathing trace amplitudes were measured using a pneumatic bellows (Lafayette Instrument). The bellows was wrapped around the patient's abdomen and as the patient inhaled and exhaled, the bellows was stretched and relaxed, causing the air pressure in the bellows to decrease and increase, respectively. A pressure transducer measured the internal air pressure and generated a voltage output, which was recorded as the breathing signal. Downstream the breathing signal and the CT scanner trigger voltage signal are collected by a multi-channel analog signal acquisition device (National Instruments). The bellows signal was synchronized to the CT-on signal from the scanner using the LabVIEW software, which allows for correlating the signal to CT slice. The breathing signal had been previously shown to be linearly related to the tidal volume [23]. The derivative of the voltage signal with time [V/s] was used as the surrogate measurement of breathing rate.

3.3 Deformable Image Registration

The acquired image data is processed using deformable image registration. Image registration is performed between a pair of images, typically termed the reference or "fixed" image and the "moving" image. The registration algorithm aligns the "moving" image to the "fixed" image while assigning motion vector to each voxel in the reference image. In respiratory motion, the lungs can undergo large and complex deformation. Accurate information on the lung tissue deformation is necessary in many clinical scenarios to ensure both accurate diagnostic assessment and treatment delivery. In radiation therapy, DIR has become an indispensable tool for estimating patient-specific motion model, which enables accurate margin definition in the treatment planning stage and ensures adequate target dose coverage in the radiation delivery. In addition, lung ventilation profile can be derived by

registering CT images at different respiration levels so that clinicians may better understand breathing disorders. Furthermore, image registration of longitudinal scans can be used to monitor the disease progression and evaluate treatment efficacy.

Typical components of a DIR algorithm include a transformation model, a similarity metric, and an optimization algorithm, all of which can affect the accuracy in image alignment. Achieving high registration accuracy in the lung is challenging due to complex deformations that occur during respiration. These complex deformations present challenges in the form of large tissue displacements, the tissue sliding motion on the lung boundaries and the strong local intensity variation caused by lung expansion and compression. In addition to these inherent issues, the registration accuracy is also highly dependent on the algorithm parameter [80, 81]. This issue has been investigated in Dou et al [82], where significant accuracy gain was found using an optimized parameter set over the non-optimized ones.

To appropriately evaluate the accuracy of the lung DIR algorithms, common data sets and comparison criteria should be employed. For example, the EMPIRE10 challenge was designed to evaluate the algorithm performance among the lung DIRs [83]. Each algorithm was tested on a variety of datasets and ranked based on boundary alignment, major fissure alignment, landmark correspondence, as well as singularities in the deformation fields.

3.4 Description of the deeds algorithm

The DIR algorithm employed throughout this dissertation was **deeds** [84-86], based on a multi-level B-spline algorithm. A unique feature of the deeds algorithm is the preservation of sliding motion near the lung boundaries, where tissues on opposite sides of the lungs can exhibit pronounced discontinuity in motion trajectories. The implementation of minimum

spanning tree derived from voxel intensity effectively separates the tissues on either side of the lung boundary and restricts the deformation vector field regularization to only apply to the voxels sharing similar intensity characteristics [85, 87]. It is worth noting that deeds algorithm accomplishes the registration of tissues near the lung interface without the use of segmentation masks and thus avoids the delay related to segmentation in the image processing pipeline. To overcome the challenge resulted from the solution becoming trapped in the local minima in the optimization process, the deeds algorithm combines the method of dense displacement sampling with a discrete optimization algorithm. This allows for registration optimization to be performed without having to form derivatives of the image similarity metric and the need for iterative solution searching. The image similarity evaluation was based on self-similarity context, which was a highly discriminative descriptor that contained structural information in the neighborhood of the voxel of interest [84, 86]. This metric was also shown to be highly discriminative in identifying anatomical features in the presence of local varying contrast and image noise during respiration as well as more accurate than mutual information, a commonly used similarity metric [86]. The registration accuracy performance of **deeds** has been validated in the recent lung specific deformable registration algorithm studies, the EMPIRE10 [83] and against the public DIR-LAB data [85].

3.5 Lung Segmentation

To assess the accuracy in the variety of lung modeling, an accurate delineation of the lung boundary is necessary. In this work, the MEVIS lung segmentation algorithm developed at the Fraunhofer Institute, Germany was employed for defining the lung masks

[88]. This algorithm was based on region growing method from coarse to fine resolution followed by morphological operations to refine the mask boundaries. The MEVIS algorithm was ranked 1st place for segmentation accuracy in the recent LOLA11 challenge.

Chapter 4

Validation Experiments of a Breathing Motion Model based 4DCT Technique

Quality assurance of 4DCT scanning can contribute significantly towards minimizing systematic errors in high precision radiotherapy of mobile lung tumors. This study explicitly tests the robustness of the model prediction accuracy in the image domain by simulating the original helically acquired free-breathing scans. The original CT scans are considered as ground truths in that they were acquired using quantitative imaging techniques that scanned each location within approximately 0.23s, so the localization uncertainty of any tissue landmark was minimal. The key distinction of the proposed workflow is that the model-based 4DCT protocol would include an accuracy assessment of the entire 5DCT workflow. To the best of our knowledge, the proposed 5DCT technique is the first respiratory-gated CT technique that explicitly estimates the accuracy of the generated breathing phase-specific images using ground truth data.

4.1 Introduction

Respiratory motion presents a significant challenge for radiation therapy because of its irregularity and the consequential uncertainty of tumor and normal organ positions, leading to larger than necessary target volumes and potentially systematic errors in radiotherapy [89]. Four dimensional computed tomography (4DCT) [44-46] has become an indispensable tool that measures and characterizes breathing-induced motion, providing

breathing phase-specific images for defining target volumes and motion mitigation strategies in radiotherapy. Ideally, incorporating 4DCT into treatment planning provides the spatial and temporal information that explicitly accounts for respiratory motion [8, 90-93].

Accurate motion estimation by 4DCT holds the potential of improving local control rates and normal tissue sparing in high-dose conformal lung radiotherapy [94-96]. However, due to breathing irregularities inherent in human quiet respiration, 4DCT is susceptible to sorting artifacts, which can cause target delineation errors [68, 74, 97, 98]. Techniques have been proposed for retrospective sorting-based approaches with the aim of reducing motion artifacts in 4DCT images [47, 72-74, 99-102]. Of these, respiratory motion model based techniques have shown promising improvement in mitigating sorting artifacts [47, 48, 73, 103], besides the additional attractive qualities of their predictive power. In particular, Thomas *et al* [103] demonstrated the generation of motion artifact-free 4DCT images at user-selected breathing phases based on a fast helical CT acquisition technique and a deformable lung motion model. The model was based on Low *et al* [50], employing two surrogates, breathing amplitude and rate, as independent variables. Such models are termed here as 5D. The model-generated 5DCT images, being sorting artifact-free, would not convey obvious indications as to whether the motion model prediction accurately reflected the phase-specific breathing motion. Ideally, the accuracy of 5DCT images would need to be evaluated prior to their clinical utilization to determine optimal motion management strategy.

In this paper, we present a technique that characterizes the accuracy of the 5DCT acquisition and motion modeling process described by Thomas *et al* [103] and Low *et al*

[104]. We proposed to use the motion model to reconstruct the original free-breathing helical CT scans for a direct comparison in the image domain. The original CT scans were considered as ground truths in that they were acquired using quantitative imaging techniques that scanned each location within approximately 0.23s, so the localization uncertainty of any tissue landmark was minimal. Using the motion model and the breathing surrogate signals measured during the image acquisition, the original CT scan geometries were simulated by deforming the reference scan image with the model-derived DVF. The original and simulated scan geometries were compared throughout the lungs using a previously validated DIR technique. Both qualitative and quantitative analyses were presented for 16 cancer patients with either primary or metastatic lung tumors.

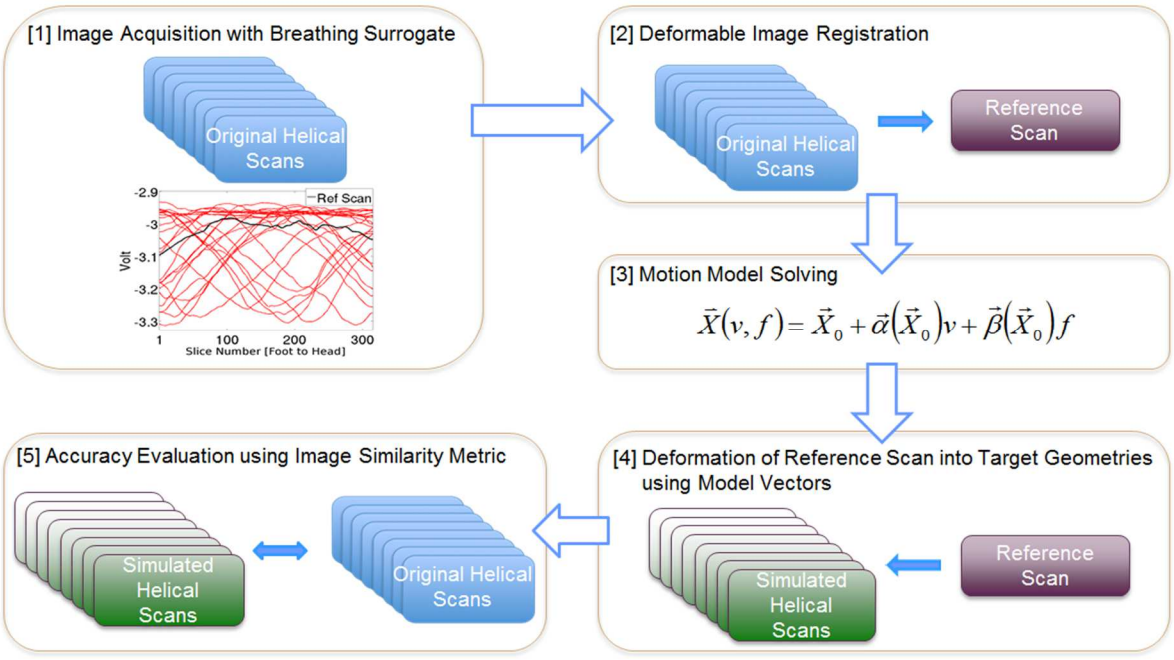

Figure 1. Flowchart of the simulation of the original scans.

4.2 Methods

Image Acquisition and Patient Lung Model Construction

Fig. 1 describes the workflow for the acquisition of the free-breathing scans and the reconstruction of these scans using the 5D respiratory motion model. Sixteen patients were imaged under an IRB approved protocol using 64-slice CT scanners (Somatom Definition Flash and Biograph TruePoint PET·CT; Siemens Healthcare, Forchheim, Germany). One patient (that would have been the 17th enrolled) was removed from our analysis because a rib was missing and the motion model was unable to manage the unusual deformation near the missing rib. To adequately sample the patient anatomy for lung model construction, 25 acquisitions of the free-breathing thoracic images were performed according to the fast helical CT protocol previously reported in [103, 104] with simultaneous recording of a breathing surrogate signal. A pneumatic accordion-shaped bellows tube was wrapped around the patient's abdomen. The tube was sealed and the air pressure in the tube monitored using a pressure transducer sampled at 100 Hz. The bellows air pressure was used as the breathing surrogate amplitude, which decreased and increased as the patient inhaled and exhaled, respectively. Using the shortest rotation period of 0.28s and pitch of 1.2, the lung anatomy was scanned through in 2.5s. Each location on the CT couch was imaged for 0.23s, short enough to be considered as essentially static representations of the patient's geometry at the time of scanning each slice. This allowed us to assign a breathing phase to each slice. The 25 helically acquired scans are termed here as the original scans. Each scan spanned a large fraction of the breathing cycle and the scans together reflected the extent of motion the lung tissues underwent. The 5DCT approach incorporated the 25 lung tissue position samples into a patient-specific lung motion model [50, 103, 104].

Lung tissue displacements were determined using DIR, where the first original scan was arbitrarily chosen as the reference image. In this common geometry, the resulting 24 deformation vector fields (DVF) were related on a per-voxel basis to the bellows-measured breathing amplitude, v, and its time derivative, the breathing rate, f, by solving the following linear equation for the lung motion model parameters [50]:

$$\vec{X} = \overrightarrow{X_0} + \vec{\alpha} \cdot v + \vec{\beta} \cdot f, \tag{4.1}$$

where $\vec{X}$ was the voxel displacement, $\overrightarrow{X_0}$ the voxel position at a zero amplitude and rate, $\vec{\alpha}$ described the motion due to breathing amplitude and $\vec{\beta}$ described the motion due to the rate-induced motion hysteresis effect.

Deformable Image Registration

The DIR algorithm employed for the study was **deeds** [84-86], based on a multi-level B-spline algorithm. Contrary to conventional thoracic registration algorithms, which relied on segmentation to model the shear motion at the lung boundary, a unique feature of **deeds** was the preservation of the sliding motion using image-adaptive minimum spanning trees [85, 87]. The incorporation of **deeds**-derived DVF into our motion modeling thus allowed for a straightforward tracking of the voxel movement on both sides of the pleural cavity. The image similarity evaluation was based on self-similarity context, which was a highly discriminative descriptor that contained structural information in the neighborhood of the voxel of interest [84, 86]. This metric was also shown to be robust in identifying anatomical features in the presence of local varying contrast and image noise during

respiration, as was typically encountered in the images obtained by our low-dose, free-breathing acquisition protocol. In a recent EMPIRE10 study [83], **deeds** achieved top-ranked accuracy in terms of landmark correspondence and had also been validated using the publicly available DIR-LAB data [85]. The use of such highly accurate DIR was essential for reducing the uncertainty in voxel position localization and contributing to the overall model parameter determination. In this work, **deeds** was used both in the initial registration of the free-breathing scans and the evaluation of matching between the simulated and original scans.

Reconstruction of Free-Breathing Scans by Lung Motion Model

We proposed that the 5DCT image accuracy be assessed by comparing between the original images and the set of simulated images generated by deforming the reference image to the same non-reference breathing phases as recorded during image acquisition. The original images and their corresponding surrogate breathing curves represented a series of respiratory states that the patient underwent during quiet respiration. Using the motion model parameters and the breathing phase information consisting of breathing amplitude and rate, the breathing phase-specific DVFs were computed according to equation (4.1) at each voxel of dimension 1 mm^3. The model DVFs pointed from the reference scan geometry to the other 24 non-reference original scans, as did the vectors obtained by the DIR process. To allow for the generation of the simulated images through resampling the reference image, the model DVFs were subsequently inverted using the fixed-point algorithm by Chen *et al* [105]. To compensate for the lung voxel intensity change during breathing, the Hounsfield units (HU) were linearly interpolated using the sampled surrogate voltages and the resulting HU correction table was applied to the lung region. The quality

of the DVF inversion was assessed by evaluating the fraction of the negative Jacobian values, which corresponded to singularities in the model-generated deformation (Table 1) [83, 105]. Lung model generated non-reference images were termed simulated images.

Statistical Analysis

For accuracy determination, the simulated images were deformably registered to their original counterparts and the resulting deformation vector magnitude of each lung voxel in the original images was used as misalignment error. For each patient, the model error was characterized using the grand mean, defined as

$$M_{GM} = \frac{\sum_{i=1}^{N} M_i}{N}, \tag{4.2}$$

where M_i was the mean misalignment error of the i^{th} scan and N the total number of scans. To provide an estimate of the worst model prediction, M_{G95} was similarly defined as the grand mean of the averaged 95$^{\text{th}}$ percentile misalignment error of all scans. To address the potential bias towards a larger proportion of lung tissues of little motion, voxels were tracked throughout the 25 scans and ratios of the mean error versus the mean displacement, defined as misalignment error ratio, were formed for each lung voxel. Two-dimensional histograms that display the misalignment error and the misalignment error ratio distributions of the lung voxels with respect to their motion were generated to analyze the motion model simulation performance. The above analysis was performed using in-house MATLAB (Natwick, MA) and C++ programs. The approximate computation times were 15 minutes for model parameter generation, 10 minutes for each deformable registration, and 3 minutes for a helical scan simulation.

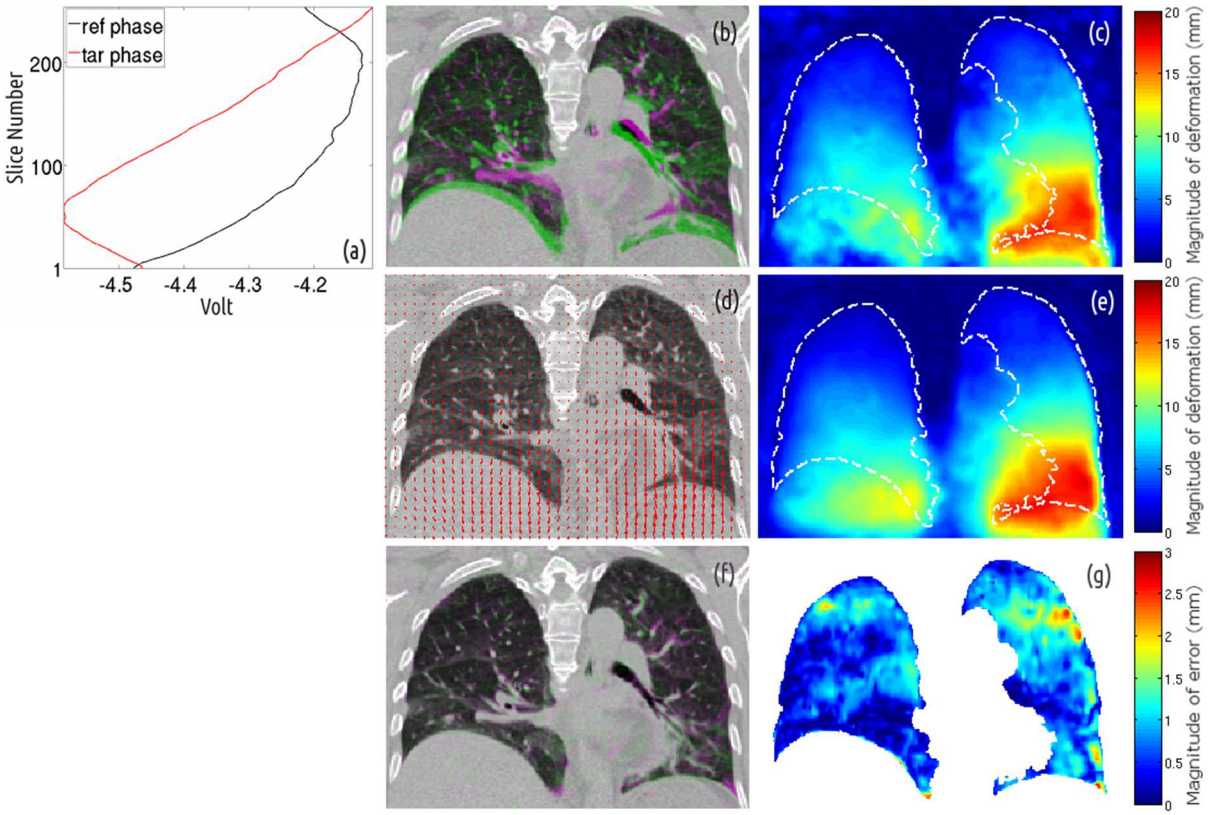

Figure 2. (a) The bellows breathing amplitude between the reference and target original scan image in patient 2. Surrogate signals of more negative voltage represents inhalation, and vice versa for exhalation breathing phases. The same convention applies to all other figures; (b) Initial misalignment between the image pair. The reference scan is displayed in green, the target scan in magenta. (c) Colormap showing the large and locally varying magnitude of inverse mapping required to create the target scan according to registration; (d) Inverted model deformation vectors overlaid on the reference image and (e) the corresponding deformation magnitude; (f) Overlay of the simulated scan onto the original scan, and (g) Residual misalignment in terms of registration deformation vector magnitude between the model simulated image and the original image.

4.3 Results

The model errors in terms of the grand mean and the grand mean of averaged 95th percentile errors are summarized in Table 1. The averaged grand mean error across the 16 patients was 1.15±0.37 mm, with the averaged grand mean of 95th percentile error estimated at 2.47±0.78 mm. Of the evaluated Jacobian values of the model generated

DVFs, the mean negative Jacobian fraction was less than 0.05% across all patients, suggesting that the inverted model DVFs were well-defined for each transformation.

Figure 2 illustrates an example of the proposed model-guided image simulation technique. For an initial misalignment between the reference scan and target original scan geometries characterized by their respective breathing waveforms (Fig 2(a)), the relative deformation was found by registering the reference scan to the target original scan. In this expanding lung deformation marked by large diaphragm displacements (Fig 2(b)), large and complex deformation was observed towards the base of the lung, where the two lungs expand by different amounts (Fig 2(c)). Subsequently, the motion model-derived DVF specific to the target breathing phase was inverted and applied to the reference image for simulating the lung deformation (Fig 2(d)). Fig 2(e) shows that the model generated deformation pattern displays a remarkable resemblance to that generated by DIR (Fig 2(c)). The excellent alignment between the original scan and the simulated one can be appreciated in Fig 2(f). Lastly, Fig. 2(g) shows the small residual differences found by forming the magnitude of the deformation vectors between the simulated and the original images, as contrasted from the initial large deformation.

Figure 3 demonstrates inter-patient examples where the 5D model accurately reproduced the tissue motion for large displacements. For 2.5s scans under free-breathing condition, diaphragm displacements of as large as 2cm relative to the reference scan geometry were accurately modeled as can be visualized by the image overlay between the simulated and the original scan. In addition, detailed lung anatomical features, such as nodules, bifurcations, lobe fissures and lung boundary, were also very well aligned. Misalignments

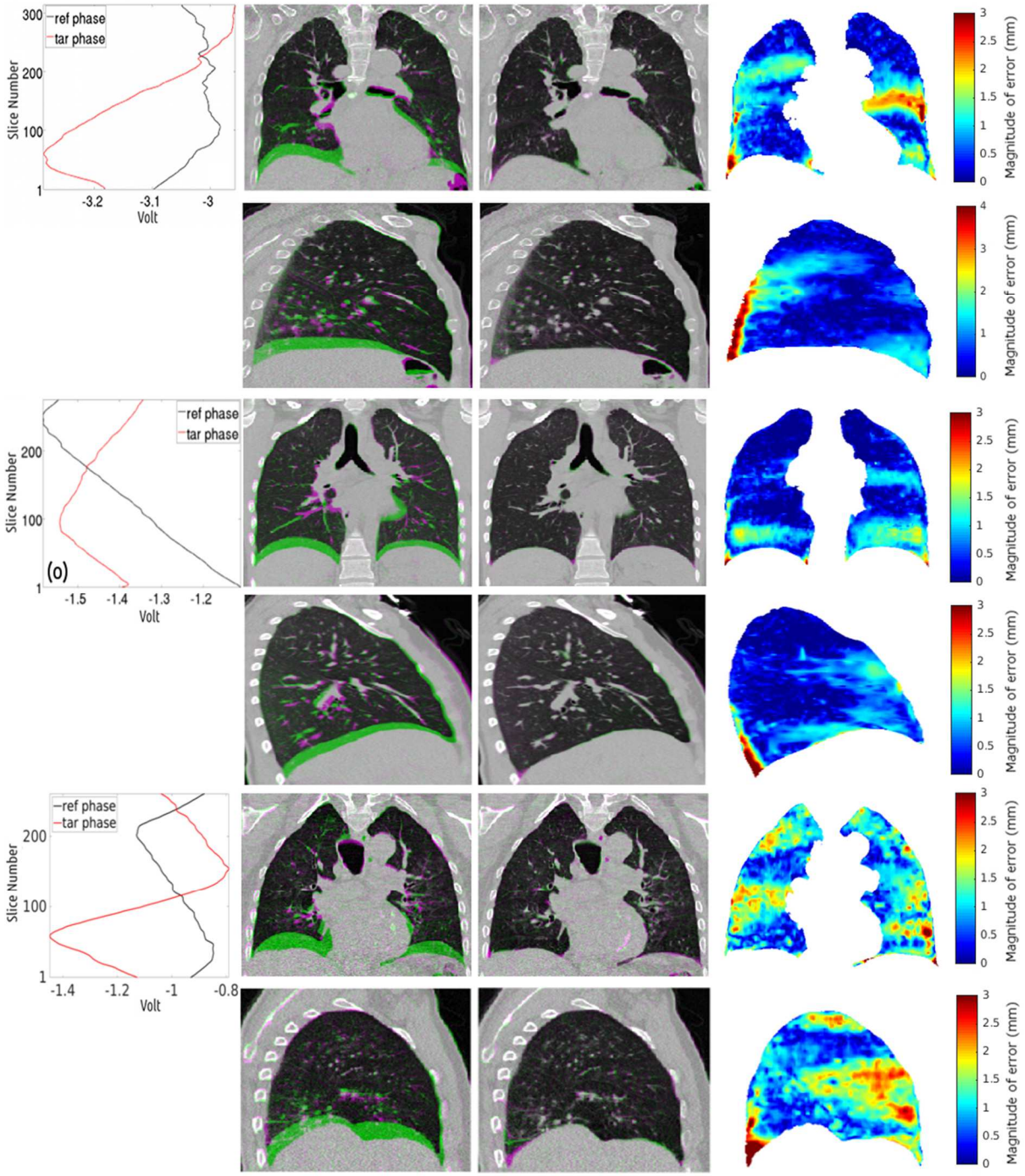

Figure 3. For patient 1 undergoing large inhalation of about 2 cm diaphragm displacement, (a) the breathing traces between the reference and target original scan; (b,c,d) the initial misalignment, the excellent alignment after applying model deformation to the reference scan, and the residual error in the central coronal slice; (e,f,g) the same in right sagittal view. Similar figures for patient 7 (h-n) and patient 13 (o-u), in large expanding deformations.

of small magnitude show regional variation in the lung and the model simulation accuracy can suffer at the lower posterior boundary of the lung. While the quantitative analysis concentrated on tissues within the lungs, the bony structures in the thorax, including the spine and ribs, were also correctly aligned due to the employed image-wide DIR technique. An example of the shear motion near the lung boundary is shown in Figure 4. Fig 4(a, b) show the positions of a lung vessel in the reference and the target original images where the target original scan was selected to reflect tidal inhalation near the diaphragm. In the close-up region, the lung vessel moved inferiorly as the lung underwent expansion. The shear motion of the cross-marked vessel within the lung boundary was exemplified by the deformation vectors pointing in inferior direction (Fig 4(e)) while the vectors outside showed little motion magnitude, displaying motion discontinuity at the chest-wall boundary. The alignment of the lung vessel in the image overlay indicated that the sliding motion on either side of the lung was well reproduced by the model.

Figure 5(a) provides the distribution of the lung voxels binned by their misalignment errors and mean voxel displacement and 5(b) the distribution of the misalignment error ratios and mean voxel displacement for patient 10. Figure 5(c) shows the distribution of the misalignment errors in patient 10 over the total number of original scans. In 5(d), a quantitative description of the error statistics for the sixteen patients was given. In all patient scans examined, the grand mean over the lung region was below 2 mm, while the grand mean of averaged 95^{th} percentile misalignment was just slightly over 4 mm.

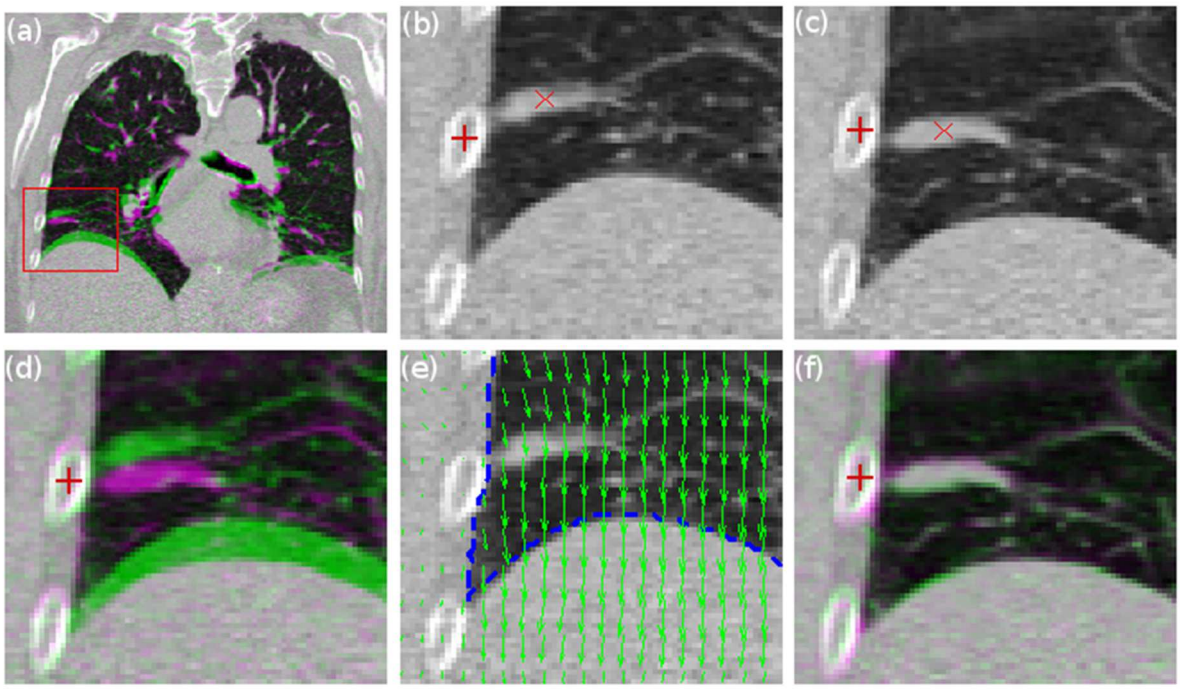

Figure 4. (a) In a patient 9 scan, where the lung is expanding relative to the reference geometry, the same lung vessel (in red box) moves in the inferior direction. A close-up of the boxed area and the position marks of the vessel (x) with respect to the neighboring rib position (+) in the reference (b) and in the target (c) and together in the overlay image (d). (e) The model deformation vectors, plotted in 4mm grid, are overlaid on the reference image. (f) The overlay image of the model simulated image on the target original image.

4.4 Discussion

A technique for characterizing the accuracy of CT images generated by the 5D model has been proposed and was tested in sixteen patients. As illustrated in Figure 5, histograms show that the vast majority of the lung voxels exhibit mismatching error on the order of millimeter. This suggested that 5DCT technique accurately reproduced the dynamic lung deformation associated with the variety of the sampled patient free-breathing states during the 2.5-minute scanning session. In particular, our results showed robustness in simulating the large deformation of deep breaths using an arbitrary reference scan.

Quality assurance of 4DCT scanning is important for minimizing systematic errors in radiotherapy of mobile tumors. Hurkmans et al evaluated 4DCT imaging accuracy using a programmable phantom that moves with periodic breathing cycle and a known motion range [106]. The present work assesses the 5DCT workflow accuracy by comparing to the high-pitch helical "snapshot" free-breathing scans as ground truth. Such accuracy assessment would be valuable in determining the appropriate motion management strategy for treatment. To the best of our knowledge, the proposed 5DCT protocol is the first respiratory-gated CT technique that explicitly estimates the accuracy of the generated images using patient ground truth data.

The validity of the original scans as ground truth was limited by the motion-induced artifacts due to high tissue motion velocities. Such artifacts appeared in some images, but consisted largely of small structure blurring (<3 mm) and ghosting of the diaphragm boundary. The position of the blurred structures, however, would generally reflect the average position of that structure during the 0.23s that the location had been scanned. We examined the CT scans and determined that the motion-induced artifacts led to relatively minor errors in the average positions of the lung tissues.

One of the hallmarks of not using time as an explicit variable was that the complexity of human breathing motion could be isolated into time-dependent and time-independent variables, where the time-dependent variable was physically measured and the time-independent variables described the spatial characteristics of the motion. This allowed breathing irregularity to be explicitly managed by the 5D motion model. The ability of the 5D motion model to reproduce lung tissue hysteresis was previously demonstrated in Thomas et al and Low et al. [50, 103]. Building on this unique characteristic, the lung

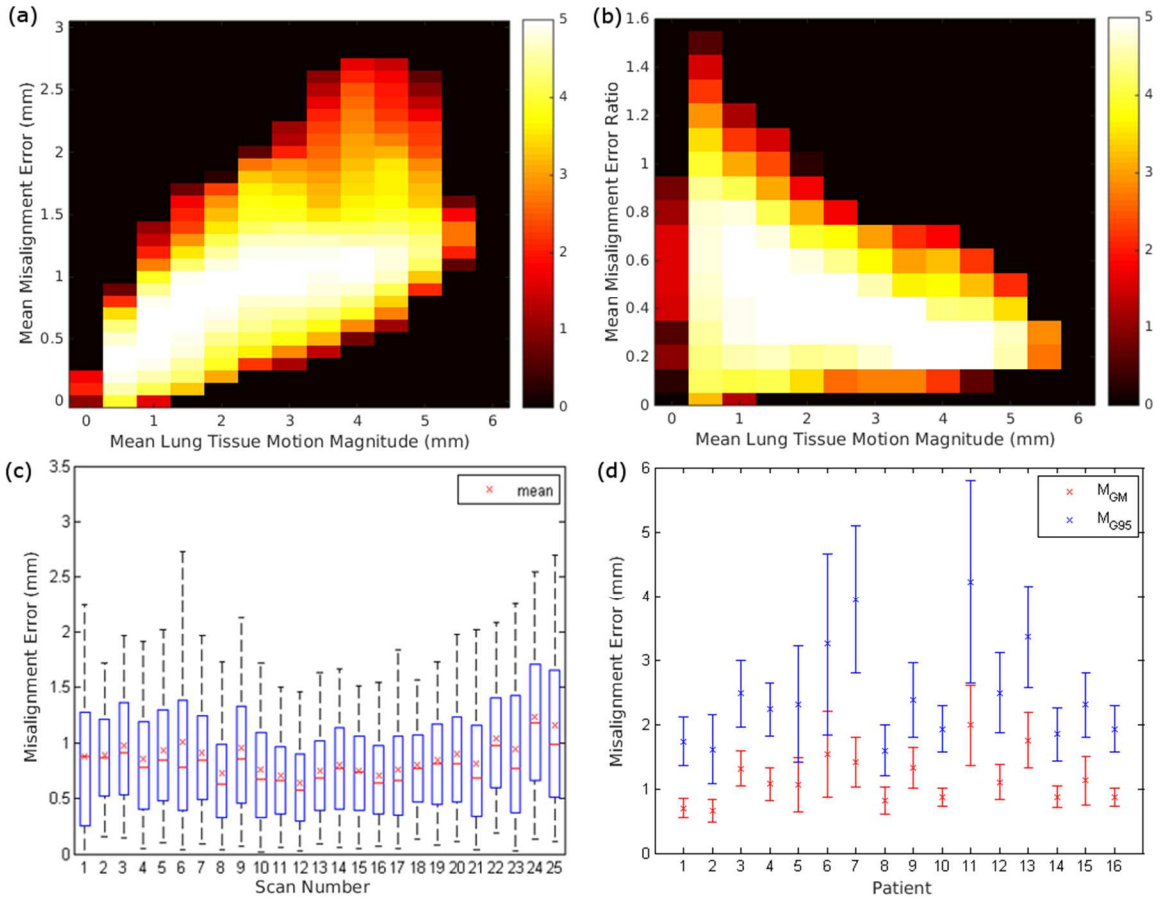

Figure 5. Histogram in a logarithmic color scale displaying for patient 10 (a) the misalignment error magnitude versus the mean motion magnitude and (b) the lung voxel misalignment error ratios versus their mean motion; (c) boxplot showing mean (x), median (red line), interquartile range (blue box), and 5th and 95th percentile misalignment error (whiskers) for patient 10; (d) distribution of the grand mean (red) and the grand mean of averaged 95th percentile (blue) error of all scans per patient, with the error bar showing the standard deviation.

modeling realism was here further enhanced by accounting for sliding motion along the lung periphery through the use of a lung-segmentation-free DIR technique. This particular modeling feature may be useful for analyzing pathologies where lung tumor is attached to the pleura and holds the potential for increased precision of highly conformal radiotherapy.

While the 5D formulation can accurately describe lung tissue motion in the examined cohort, the accuracy of the simulated tissue alignment was specific to the patient, the breathing phase, and also showed local variation throughout the lungs. For example, the larger misalignment errors observed in patient 11 can be attributed to the fact that most breathing signals were captured during exhalation phases. This has compromised the model's ability to extrapolate to the deformation of deeper breaths in this patient. A prospective CT acquisition technique that assures adequate breathing phase sampling for each location in the lung will be developed to address this issue. The measurement noise in the surrogate signal is found to be correlated with the increased misalignment error, particularly in patients 6, 7, 11, and 13. The high frequency components in the recorded physiological signal introduce uncertainties in the model parameter determination and degrade the reproducibility of tissue positions in the original scan images, especially if the reference breathing signal suffers from such noise. Careful placement of the abdominal belt and dedicated circuit design can potentially improve the surrogate measurement. The model accuracy suffered towards the posterior lung boundary, likely because the tissue motion tended to be greatest in this region with subsequent motion-induced blurring in the images acquired during inspiration or expiration. The blurred images would be more poorly registered relative to images acquired during peak inhalation or exhalation. The image acquisition-related issues of posterior edge misalignment and artifact errors could in the future be minimized by scanning at higher pitches, faster rotation speeds, or using more sophisticated image reconstruction.

4.5 Conclusion

We have demonstrated a method that evaluated the accuracy of a 5DCT technique by comparing the model-simulated images against the ground-truth original scanned images. The demonstrated similarity agreement for the examined large deformations during free-breathing imaging suggested the applicability of the proposed 5DCT technique for a wide range of patients. The proposed ground truth based analysis is unique in CT-based breathing motion modeling for radiation therapy and will provide uncertainty estimations in the model-based 4DCT breathing motion estimate of tumors and normal organs.

Chapter 5

Characterization of Lung Tissue Density Change during Free Breathing

Accurate accounting of dynamic lung density variation is desirable and forms the basis for treatment planning calculations. In charged particle radiotherapy, accounting for lung density variation is particularly crucial for ensuring accurate treatment delivery. This work investigated a functional relationship that calibrates the density change of the human lung tissues under free breathing conditions. This was accomplished by processing snapshot images of the lung scanned by fast helical CT technique using highly accurate deformable image registration. Our proposed density calibration approach couples the motion vector field to the tissue density assignment and allows for the tissue density to be assessed directly through the computation of the determinant of the Jacobian matrix. The proposed density calibration scheme is general, patient-specific, and can be applied to any lung motion models that generate lung images using motion vector field. We envision the presented method can be applied to SBRT and particle radiotherapy in the thorax and will be a key enabling technique for 4D lung treatment planning techniques that require accurate lung anatomical and density representation and Monte Carlo based dose calculation. In addition, if follow-up fast helical scans become available, our technique can potentially be used for dose response modeling.

5.1 Introduction

In radiation therapy, the accuracy and precision of the treatment planning process is important for achieving adequate target coverage and avoiding healthy tissues. In thoracic radiation therapy, 4D imaging has been introduced to provide lung density information over the different breathing phases in the breathing cycle. However, due to image sorting artifacts, irregular patient breathing makes 4DCT prone to inaccurately characterizing lung density variations [107]. Human lungs contain significantly heterogeneous tissues with an average density one third of that of water. In a lung phantom study by Aarup *et al* that examined the dependence of dose difference on density variation [108], Monte Carlo calculations demonstrated that when decreasing the lung density from 0.4 to 0.1 g/cm^3, the median dose to the target decreased by up to 15% and more than 20% for 6 MV and 18 MV photon beams, respectively. However, few studies to date have systematically investigated lung density changes during quiet respiration using human data.

Modeling of lung density changes during the breathing cycle has often been performed based on the principle of mass conservation. McGurk *et al* [109] modeled density change based on the conservation of global lung mass and applied a mean lung density throughout the lungs specific to each breathing phase. Williams *et al* [110] proposed a density correction scheme by combining the voxel Hounsfield units (HU) values of the reference phase image and the volume change was computed using the divergence of deformation vectors around the voxel of interest. Both of these studies were performed using computational phantoms. The accuracy of such density assignment, however, has not been validated in humans.

In this study, we present a technique that characterizes the density change of lung tissues during quiet respiration using free-breathing patient data. A series of free-breathing lung

image CT scans were acquired using a fast helical protocol [103, 104] such that the lung tissues were imaged with minimal motion-induced blurring or artifacts. Deformable image registration was performed on the image data, and the obtained deformation vector fields (DVF) were subsequently used to compute the Jacobian map whose voxel values estimated the voxel-specific volume change. Tissue specific functional relationships that described the density change during free breathing were obtained by correlating the set of HU intensities with the Jacobian values for each voxel using least square fitting. Through testing the mass conservation assumption, we differentiated the lung tissues according to the observed data fitting performance and devised a scheme that separately modeled the density variation for each classified tissue types present in the lungs. The model-generated density values were examined with the acquired CT image data and also validated using a leave-five-out cross validation method. To our knowledge, this is the first work that models the dynamic local lung tissue density change during quiet breathing based on patient image data.

5.1 Methods

Image Acquisition

The fast helical CT protocol [103, 104] was originally developed to provide multiple samples of tissue position during free-breathing for modeling lung tissue motion. The image acquisition was performed using a 64-slice Siemens Definition Flash (Siemens, Forchheim, Germany). Our proposed technique was conducted on a subject that underwent the fast helical CT protocol that scanned the lung anatomy 25 times, each scan taking 2.5s. The scanning was performed employing a pitch of 1.2 and rotation time of 0.28s so that

each piece of lung tissue was imaged for approximately 0.23s and the images were reconstructed using the Siemens B30f reconstruction kernel with a voxel size of $1 \times 1 \times 1$ mm^3 [103]. Thus, the images represented the lung anatomy throughout the sampled portions of the patient breathing cycle. Each scanned image slice was considered to approximate a static snapshot of the lung.

Deformable Image Registration and Jacobian Computation

To provide a common geometry for image analysis, the acquired free-breathing images were registered to a reference image, which was arbitrarily assigned as the first scan. The deformable image registration employed for this work was the deeds algorithm [84, 85, 111]. Using self-similarity context, the algorithm evaluated image similarity based on the neighborhood intensity structure around the voxel of interest. Deeds has been validated in the recent thoracic deformable registration evaluations using the public DIR-LAB data [85] and has achieved the second best target registration error in the EMPIRE10 challenge [83]. The deformed non-reference images generated by the registration algorithm contained the interpolated HU values of each tracked reference image voxel in the non-reference images. The Jacobian was calculated for every voxel by estimating the local affine transformation matrix, which transformed the reference image coordinates to the deformed image coordinates, and calculating the determinant of the resulting affine matrix. The accuracy of the Jacobian computation was validated through the lung volume comparison in the registered image pairs. For a pair of test images that involved 24% volume change, in terms of the number of voxels within the lungs, the difference in voxel counts between the segmented moving image and the integration of Jacobian values over the deformed moving image was 0.2%.

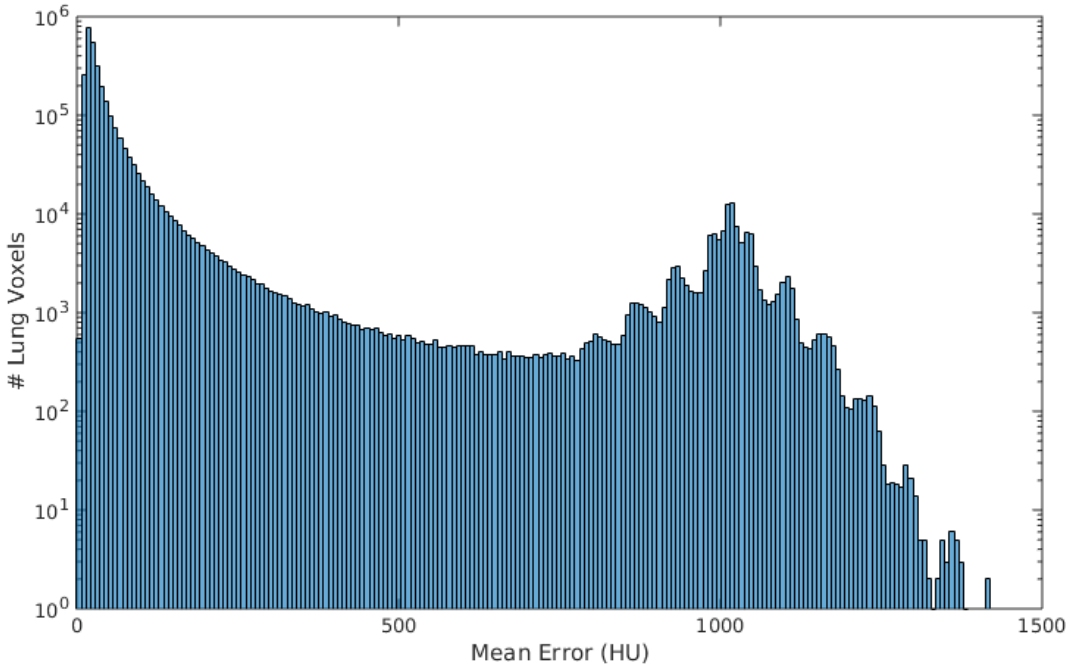

Figure 1. An error histogram obtained by applying mass conservation fitting to the Jacobian and HU for each lung voxel. This histogram is plotted in logrithmic scale.

Data Analysis and Density Model

The lungs were segmented using a highly accurate segmentation algorithm [112]. The basis of our modeling assumption was that the mass of the voxel content was conserved between each pair of reference and non-reference images and only the volume and density changed such that $\rho_1 v_1 = \rho_2 v_2$. The physical density of the lung tissue was related to the radiological attenuation coefficient [113] as

$$\rho = \frac{HU}{1000} + 1. \tag{5.1}$$

The local volume change due to the deformation could be approximated using the determinant of the Jacobian of the transformation field, $\frac{v_2}{v_1} \cong \det \nabla\phi \equiv J$ [114]. The local mass conservation relationship could therefore be expressed as

$$\frac{\frac{HU_2}{1000}+1}{\frac{HU_1}{1000}+1}\cdot J = 1 \tag{5.2}$$

Since the HU value of reference voxel stays the same for our 25 data points, Eq (5.2) was simplified to

$$(\alpha \cdot D + \beta)\cdot J = 1, \tag{5.3}$$

where D represented tissue density in HU, α had units of 1/HU and β was unitless. α and β were fitting coefficients that related D to the Jacobian. To ensure the association of large and negative HU values to increasing Jacobian values, α and β were obtained by fitting HU_2 and $1/J$ using constrained least square optimization for which $\alpha > 0$. The term $\alpha \cdot D + \beta$ expressed the density change ratio relative to each reference image voxel and Eq (5.3) imposed the mass conservation relationship on the fitted curve, characterized by α and β. The obtained α and β represented the underlying density pattern. In particular, the fit constant α determined the curvature of the resulting fitted curve. The application of Eq (5.3) to correlate the Jacobian to the HU values resulted in the error histogram over the entire lungs in Fig.1. The histogram analysis shows that about 80% of the total lung voxels have mean errors up to 60 HU. In addition, the shape of the error distribution indicates that mass conservation fitting alone cannot account for the density change and indicate that additional modeling is required to describe the density change pattern. In Fig. 2, a careful inspection of the coefficient α map led us to classify the voxels with values greater than 0.001 as type I, values between 0.001 and 0.0001 as type II, and values between 0.0001 and zero as type III. Separate fitting schemes were applied to each region and took on the following forms,

$$Type\ I\colon\ \alpha\, D + \beta = \frac{1}{J}, \tag{5.4a}$$

$$Type\ II\colon\ \ D = \gamma\, J + \delta, \tag{5.4b}$$

$$Type\ III\colon\ D = \varepsilon, \tag{5.4c}$$

where γ and δ represent the linear fitting coefficients, and ε the averaged value of the voxel HU. The inverse linearity assumption for type II tissues applied mostly to the region of lung vessels. Our assumption was supported by the volume change of the pulmonary vessels reported in literature [14,15]. In particular, Clark et al [14] stated that "Extra-acinar vessels, which are embedded within and tethered to the parenchymal tissue, are distended axially and radially on inflation, …". This physiological observation allowed us to correlate the changes in HU with the volume changes in the lung vascular tree. Type III was designated to address the remaining portion of the lung tissues whose density variation appear to be independent of the Jacobian values and was modeled to have constant density value obtained by averaging all data points.

To evaluate the accuracy and the variability of our model, one hundred trials of leave-five-out experiments were performed, where a random subset of 20 out of the 25 scans were selected as training data for coefficient estimation, and the Jacobian values from the remaining 5 scans were used to calculate and predict the modeled densities via the obtained fitting parameters and these compared with the acquired density data. The mean absolute differences between the modeled and experimental HU values were computed for each voxel. To assess the intrinsic image noise, a region in the trachea filled with air was selected to evaluate the image intensity uniformity and the standard deviation of the HU values was found to be around 30 HU.

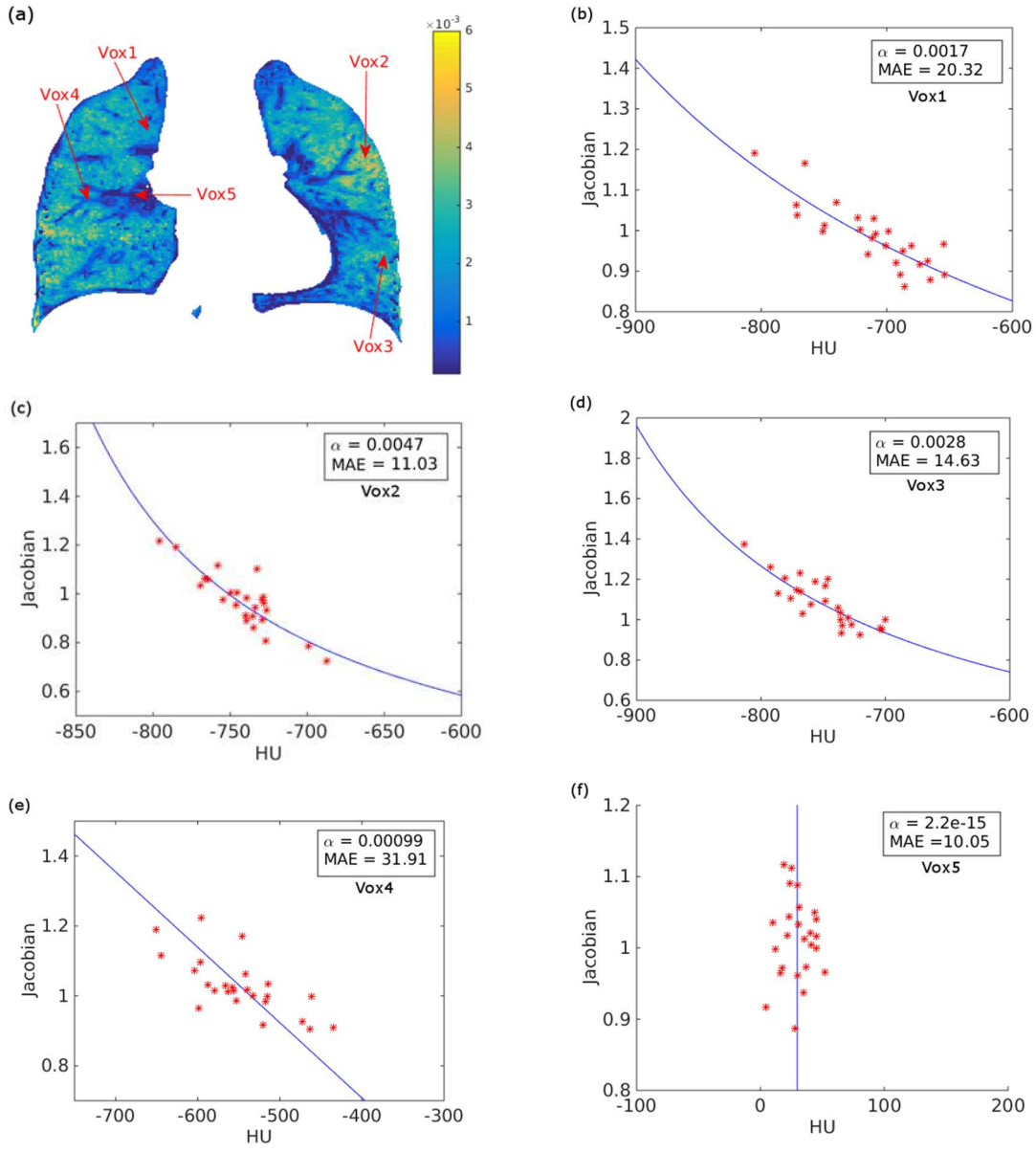

Figure 2. (a) spatial map of the fitting coefficient α; (b-f) scatter plots of the 25 point pairs of Jacobian versus HU for the labeled example voxels on the central coronal slice, plot legend specifies the fitting coefficient α for tissue classification and the evaluated mean model error.

The above analysis was performed using the MATLAB software (Natwick, MA).

5.3 Results

In Fig. 2, the distribution of the obtained fit constant α showed local variation. The magnitude of the fitting coefficients revealed the underlying trend in terms of the mechanical properties of the lung tissue, ranging from those that obey the mass conservation relationship to those subject to elastic expansion and contraction and finally those that are not sensitive to Jacobian change, such as the soft tissues in the interior of the large lung vessels. Type I tissues corresponding to lung parenchyma also exhibit different density characteristic profiles marked by the different levels of α values as shown in Fig 2 (b-d). Fig 2(e) and (f) show example voxels of Type II and Type III tissues according to our classification scheme by mass conservation fitting and the subsequent modeling and accuracy evaluation.

Fig. 3(a) shows a coronal CT slice through the reference image, 3(b) shows the defined tissue types, 3(c) shows the range between the maximum and minimum HU values for each voxel, and 3(d) the computed mean absolute error of the density model over the 25 scans. Upon comparing Fig 3(a) and 3(b), one can appreciate the rendering of the lung vessel tree distribution, suggesting that classification by thresholding the initial mass conservation fitting coefficient, α, can effectively distinguish between the parenchymal and vessel tissues. The intensity distribution in Fig 3(c) indicates that lung vessels undergo greater density change than the parenchyma tissues, although the latter can exhibit regional

variation. Fig. 3(d) shows that the mean residual error after applying our calibration scheme.

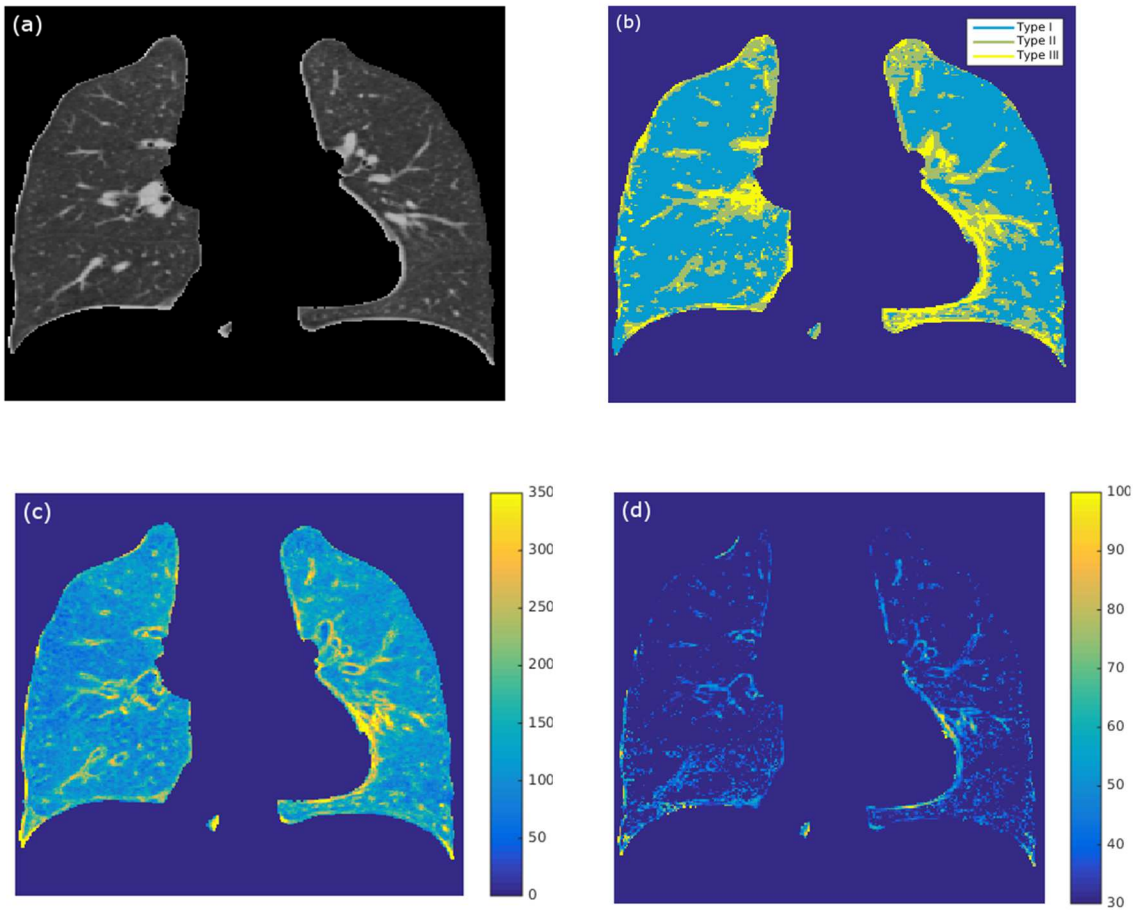

Figure 3. In the mid-coronal slice, (a) The reference image; (b) The distribution of the lung tissue types, I. parenchyma, II. vasculature, III. soft tissue; (c) The range of lung density in HU observed in the 25 fast helical scans; (d) The resulting mean absolute error in the lung after applying the density calibration method.

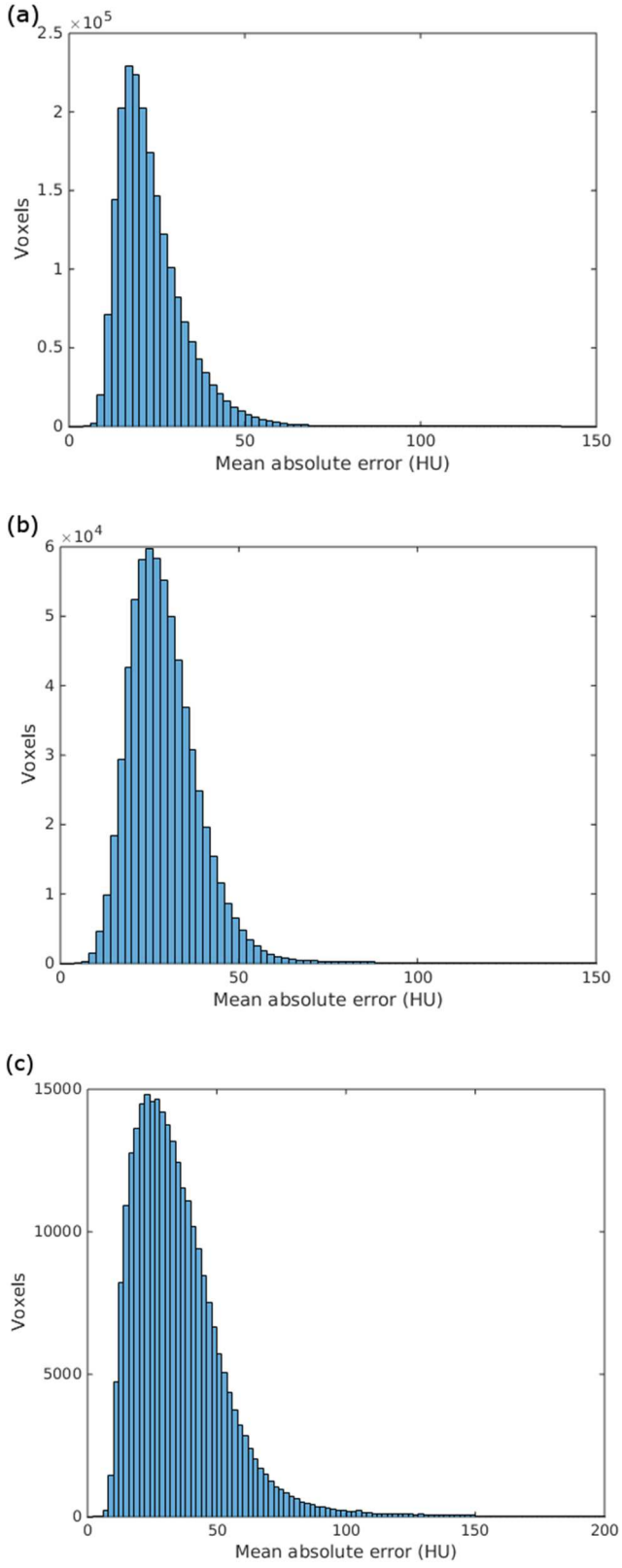

Figure 4. The histogram distribution of the mean absolute error in region I (a), II (b), and III (c) using data from the 25 scans.

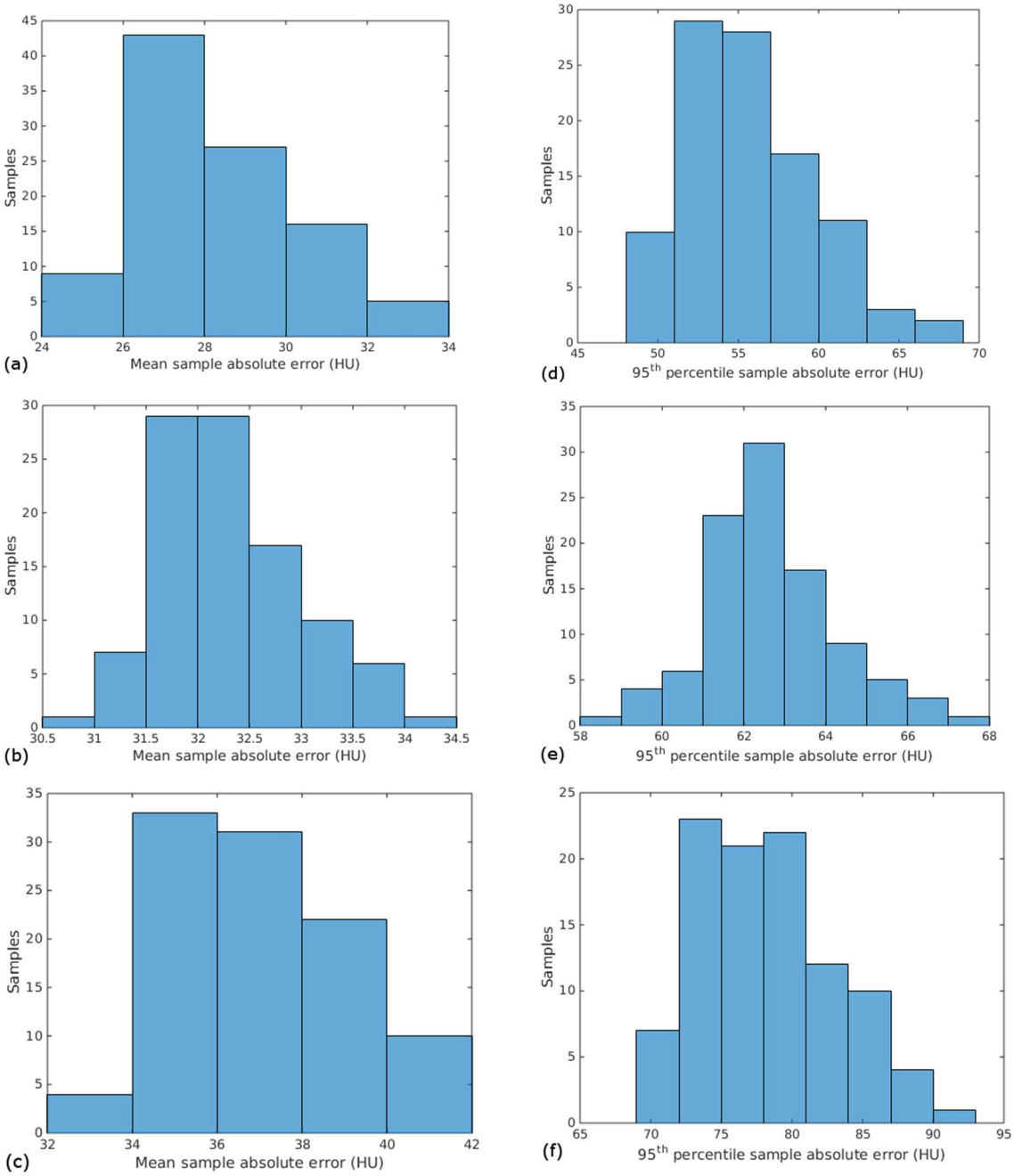

Figure 5. Histogram of the mean absolute error in HU for the leave-5-out experiments in region I (a), II (b), and III (c). Histogram of the 95th percentile absolute error in HU for the leave-5-out experiments in region I (d), II (e), and III (f).

Table 1. Statistics of the validation experiment

Error	mean (HU)	95%-ile (HU)
Region I	28.31 ± 2.07	55.62 ± 4.06
Region II	32.32 ± 0.66	62.65 ± 1.60
Region III	37.05 ± 2.15	78.15 ± 4.85
Total	30.02 ± 1.67	59.94 ± 3.15

Fig. 4 shows the distribution of the model error for each of the three modeled regions. The mean errors for regions I, II, and III were 23.30±9.54 HU, 29.31±10.67 HU, and 35.56±20.56 HU, respectively. The error distributions in the three regions appeared to peak at around 30 HU. Both the small mean value of around 30 HU and the small standard deviation for each of the distributions indicated the model quality. Fig. 5 shows the error histograms both in mean model error and 95th percentile model error for the hundred validation experiments. The model error statistics are shown in Table 1. The mean model error distributions were found to be centered around 30 HU, confirming the model results using the full 25 scans.

5.4 Discussion

Our proposed density calibration approach couples the motion vector field to the tissue density assignment and allows for the tissue density to be assessed directly through the computation of the determinant of the Jacobian matrix. The density calibration scheme classified the lung tissues into three categories based on their fitting characteristic to the mass conservation relationship. Subsequently, we categorize lung tissues into lung

parenchyma (Type I), lung vessels (Type II), and soft tissues or air (Type III), which account for, 70%, 20%, and 10% of the total lung volume, respectively, according to the employed lung segmentation. In the parenchyma region, tissues show local variation in terms of their fit coefficient α; as observed in Fig. 2 (b,c,d), the voxels with greater α values exhibit greater volume changes, suggesting their stronger involvement in air exchange during respiration, and vice versa for those with smaller α values. The correlation of the regional variation in α with local ventilation estimation will be the subject of a future investigation. The Type II tissues are modeled to undergo density changes that are inverse linearly related to the Jacobian. The lung vessels here refer to the extra-acinar vessels whose dimensions can be detected within the image resolution of our imaging protocol. Our approach is consistent with pulmonary physiology where the elastic materials in the lung parenchyma exert tethering forces on the neighboring lung vessels [115]. Since the tethering effect applies to both blood vessels and the bronchial airways, we do not make a distinction between the two types of vessels in terms of their response to the Jacobian values.

The resulting error distributions appear to be random and without regional dependence. Noticeable residual error can sometimes be found along the traces of the vessels, which may be caused by the partial volume effect at the steep density gradient vessel-interstitium boundary in the interpolation process. A finer voxel dimension in the image reconstruction could perhaps improve the accuracy in these areas. Another region prone to reduced model accuracy is the region near the heart, where cardiac motion may cause imaging artifacts that affect the registration accuracy. This motion-induced error can be mitigated through scanning patients using faster couch motion in future generations of the CT scanner. The

sampling of the lung tissue density range can be further improved through prospective CT imaging where the image acquisition is gated on the monitored tidal volume.

The presented lung density analysis concerns a broad spectrum of scientific specialties, including but not limited to lung physiology, image acquisition, reconstruction and registration, and radiation therapy. In radiation therapy, accurate accounting of the lung density during breathing forms the basis for accurate dosimetric analysis of lung radiotherapy. Stereotactic body radiation therapy (SBRT) has shown improved thoracic cancer treatment outcomes [3]. However, given the low-density, high-heterogeneity, complex nature of the lungs, the high-dose and small field treatment modality of SBRT presents a significant challenge for an accurate dose calculation since a) the low-density medium allows for high radiation transmission and low radiation interaction and b) small radiation field violate the charged particle equilibrium condition. Accurate and precise electron density information underlying the lung image intensity is thus desirable for treatment planning purposes. In charged particle radiotherapy, accounting for lung density variation is particularly crucial for ensuring accurate treatment delivery [116]. The proposed density calibration scheme is general, patient-specific, and can be applied to any lung motion models that generate lung images based on modeled motion vector field [104, 117]. While our proposed methodology would benefit patients in lung radiotherapy, it can be utilized in other clinical scenarios that involve radiation delivery through the thoracic cavity, such as radiosurgery of the heart or esophagus. We envision the presented method will be a key enabling technique for 4D lung treatment planning techniques [118, 119] that require time series' of accurate lung anatomical and density representation and Monte

Carlo based dose calculation. The application of the proposed density calibration technique is currently investigated using a realistic lung motion model.

5.5 Conclusion

Human lung tumors present a serious challenge to radiation therapy because of the inhomogeneous tissues present and the large density changes the lungs undergo during breathing. We have presented a technique that uses the geometrical volume change information to predict the density change during quiet free breathing. The density calibration model accuracy is demonstrated using a patient CT data and the error is found to approach the limit of the background image noise. The proposed technique provides a valuable tool for performing human lung density analysis and may find important applications in pulmonary medical physics.

Chapter 6

Characterization of Lung Ventilation and Dynamic Lung Ventilation Mapping

Recent technical advances in multi-slice detector CT scanner enable unprecedented spatiotemporal resolution due to the improvement both in reduced rotation time and increased detector coverage. The improved image quality holds great potential for investigation in pulmonary functional imaging such that the functional information may be corresponded with structural detail. 4DCT provides the spatio-temporal distribution of the cancerous tissues. In planning the radiation treatment, the information of pulmonary function should be taken into account as it may constitute additional constraint for the dose distribution. While studies have shown the feasibility of generating ventilation maps directly from 4DCT, such approaches may be limited by the use of only extremal breathing phases and image artifacts. This chapter aims at characterizing the regional lung ventilation mapping using the multiple fast helical CT scans and presents a robust statistical technique for estimating the lung ventilation. In addition, dynamic lung ventilation maps evaluated at different tissue expansion levels are also presented.

6.1 Introduction

The primary function of the lung is gas exchange. Functional information of the lung, such as ventilation and perfusion, is desirable in the patient treatment workflow in that it allows for pre-treatment therapy design and post-treatment disease progression monitoring. To

this end, the advance in medical imaging sees different techniques being implemented. These include PET, MR, SPECT, and CT, each with its advantages and disadvantages [ref]. Recently, multiple studies have used 4DCT image series to derive ventilation imaging and shown that the lung ventilation profile is highly correlated to that obtained from other traditional imaging modalities, such as PET and SPECT [120-123]. 4DCT based ventilation imaging has also been directly validated against lung functional test [124]. In thoracic radiotherapy, ventilation imaging may also yield valuable information for treatment planning so that regions of high ventilation can be appropriately accounted for in the dose calculation [125, 126]. In addition, 4DCT ventilation imaging has also seen application in monitoring changes in pulmonary function following radiation therapy [127]. 4DCT derived ventilation imaging is a promising technique in many clinical applications. In comparison to other modalities, 4DCT ventilation imaging has advantages in its high resolution pulmonary functional information that directly corresponds to the anatomical details, in addition other benefits including high signal to noise ratio, faster imaging time, and greater availability to patients. Prior to its clinical utilization, the accuracy of these ventilation images should be evaluated against ground truth. The generation of ventilation images has typically been performed through deformable image registration and Hounsfield unit analysis on the peak exhalation and inhalation images [128]. However, the image artifacts due to respiratory motion can adversely affect the accurate ventilation characterization and remain to be addressed [129]. The purpose of this study was to investigate a novel approach to characterizing patient ventilation pattern using a recently developed high pitch helical CT protocol and rigorous statistical technique to derive the most probable tissue ventilation profile with multiple samples of artifact free image data.

In addition, we evaluate the effect of motion artifacts by comparing ventilation images obtained using conventional 4DCT approaches and those from our method.

6.2 Methods

CT Image Acquisition

Fast helical CT imaging protocol was performed in 10 patients with lung cancer. A total of 25 scans were acquired to ensure adequate sampling of the lung anatomy under free-breathing condition. The results from one example patient were shown to demonstrate the feasibility of our technique. The scan direction was alternated to ensure fast scan time. The CT scanning was performed on 64-slice CT system (Somatom Definition Flash and Biograph TruePoint PET·CT, Siemens Healthcare, Forchheim, Germany), where the following scanning parameters were used: collimation width of 3.84 cm, 0.28s gantry rotation time, pitch of 1.2, and 120 kVp tube voltage. Each scan of the patient thorax takes about 2.5s, and the irradiation time of each slice was 0.23s.

Deformable Image Registration

The fast helical CT images were processed using the deeds deformable registration algorithm [85]. The deeds algorithm has achieved state-of-the-art registration accuracy in the recent lung specific EMPIRE10 Challenge in terms of landmark-based error evaluation. It has also been separately validated using the public DIR-LAB 4DCT datasets and achieved sub-voxel level error.

The deeds DIR is a multi-resolution, B-spline based algorithm. The deeds algorithm accounts for the sliding motion that occurs along the lung boundary through the use of

minimum spanning tree. As similarity metric, it employs the self-similarity context, which incorporates the intensity information in the local neighborhood for voxel matching evaluation. Thus, SSC is independent of the local contrast and image noise and is highly discriminative of different image features. Furthermore, in the registration optimization process, deeds algorithm employs a novel discrete optimization scheme, which allows for the solution finding process to be efficient and to avoid the local minima of the cost function.

Ventilation Pattern Computation

Lung ventilation image can be considered as regional mapping of the extent of regional tissue expansion under normal breathing condition. To quantify such extent of tissue expansion, in the following, we introduce a novel probabilistic formulation for estimating regional ventilation from the sampled tissue-specific data. With respect to the voxel in the reference image, the set of 24 corresponding Jacobian values, $X_1, X_2, \dots, X_{24}$, are different sampled values of tissue volume change. We assume that each of the independently measured Jacobian values shares the same distribution. Thus, to estimate the lung tissue ventilation, we are interested in evaluating the expectation value of the range of X. Let $X_1, X_2, \dots, X_{24}$ be independent, identically distributed random variables, each with the same cumulative distribution function, $C_x(x) = P(X_i \leq x)$. Let Y be the maximum of the random variable,

$$Y := \max\{X_i\}. \tag{6.1}$$

The probability function, P, of Y at a specific value x is then

$$P(Y \leq x) = P(\max(X_i) \leq x). \tag{6.2}$$

The cumulative probability function, C, can be obtained by

$$C(Y \leq x) = \prod_i P(X_i \leq x), \tag{6.3}$$

where the probability distribution *P* can be found empirically through

$$P(X_i \leq x) = \frac{\sum_{i=1}^{24} I(X_i \leq y)}{24} \tag{6.4}$$

The same process was repeated to find the minimum of voxelwise Jacobian distribution. The expectation value was computed for both the voxel maximum and minimum distributions. The ventilation image was subsequently obtained by taking the difference of the expectation values of the maximum and minimum. The technique of evaluating the range of expected Jacobian minimum and maximum values is termed statistical Jacobian ventilation.

Ventilation Pattern Comparison

In literature, besides the Jacobian based metric, the Hounsfield intensity values have also been employed for estimating the ventilation properties [85, 122, 130]. In such approaches, images at different breathing phases are typically registered to the full exhalation phase. The local fractional volume change can be represented by the fraction of air in the CT volume element as follows [85],

$$\frac{\Delta V}{V_{ex}} = \frac{I_{ex}(x) - I_{in}(x+u)}{I_{in}(x+u) + 1000}, \tag{6.5}$$

where ΔV represents the local change of lung volume, V_{ex} the exhale volume, I_{ex} the exhalation image and I_{in} the inhalation image, u the displacement vector with respect to the exhalation image. As this definition follows from the extremal breathing phase

definition in 4DCT, the exhale and inhale intensities were taken from the sorted maximum and minimum voxel intensities. The estimated ventilation values were processed using a 7mm x 7mm x 7mm median filter to remove image noise. However, it has been found that transformation based ventilation estimation was more reproducible than the intensity-based approach [131].

6.3 Results

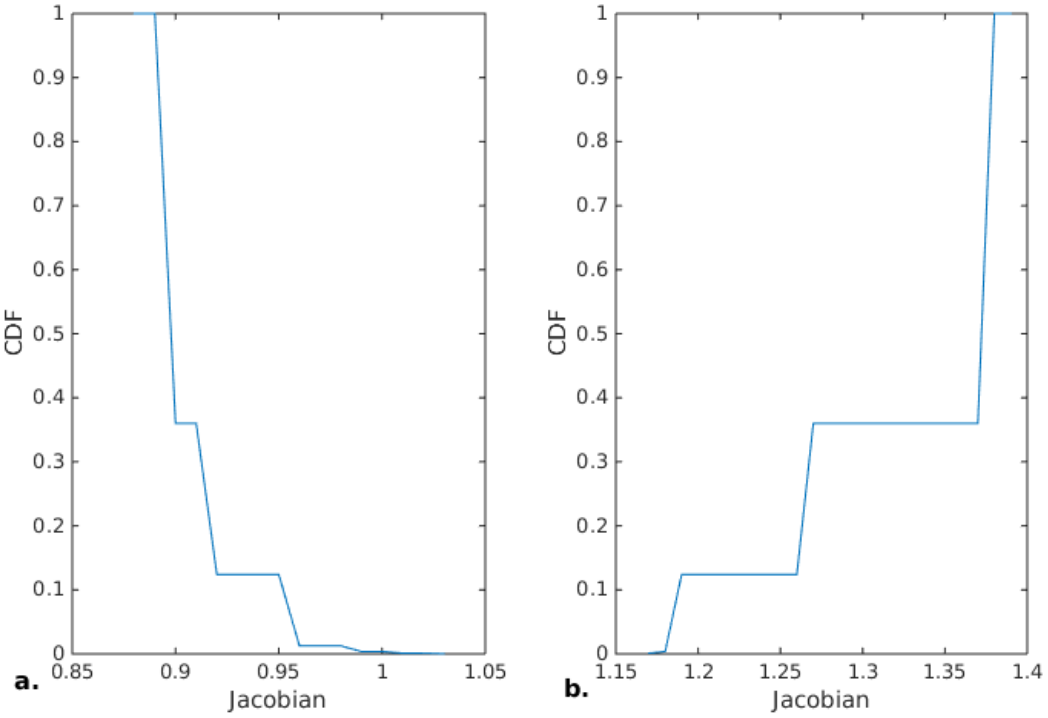

Figure 1. The cumulative probability distribution of the minimum and maximum Jacobian value for an example lung voxel.

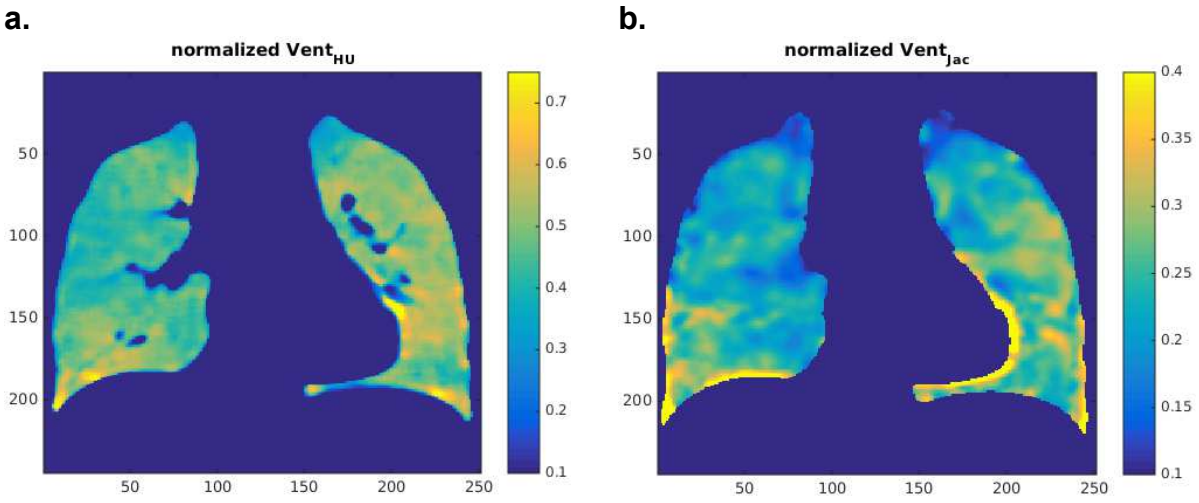

Figure 2. A comparison of the ventilation profiles between the two approaches: HU vs. Jacobian. Both images were normalized to their maximum value.

Figure 1a and 1b show the cumulative probability distributions of the minimum and maximum Jacobian values of an example lung voxel, respectively. Expectation values were computed from the inner product of the Jacobian and the probability arrays.

Figure 2 shows the comparison of the ventilation estimation found through the HU approach and the proposed statistical Jacobian approach. The ventilation pattern between the two images shows good regional resemblance. Our statistical ventilation image also correctly showed low level of ventilation where pulmonary blood vessels reside. As our approach does not require the pre-processing of removing blood vessels, HU intensity based image shows low ventilation levels in the vicinity of pulmonary vasculature, as should be expected. Our statistical Jacobian ventilation images show a more smooth appearance.

Nonparametric Spearman test shows a correlation score of 0.45 between the two data sets. Figure 3 shows a quantitative comparison between the two techniques in terms of 2D histogram analysis, normalized each to their maximum values. The great majority of the

evaluated lung voxels shows strong correlation evidenced in the trend of large voxel accumulation centered at around 0.5 in the Jacobian metric and 0.25 in the HU based metric.

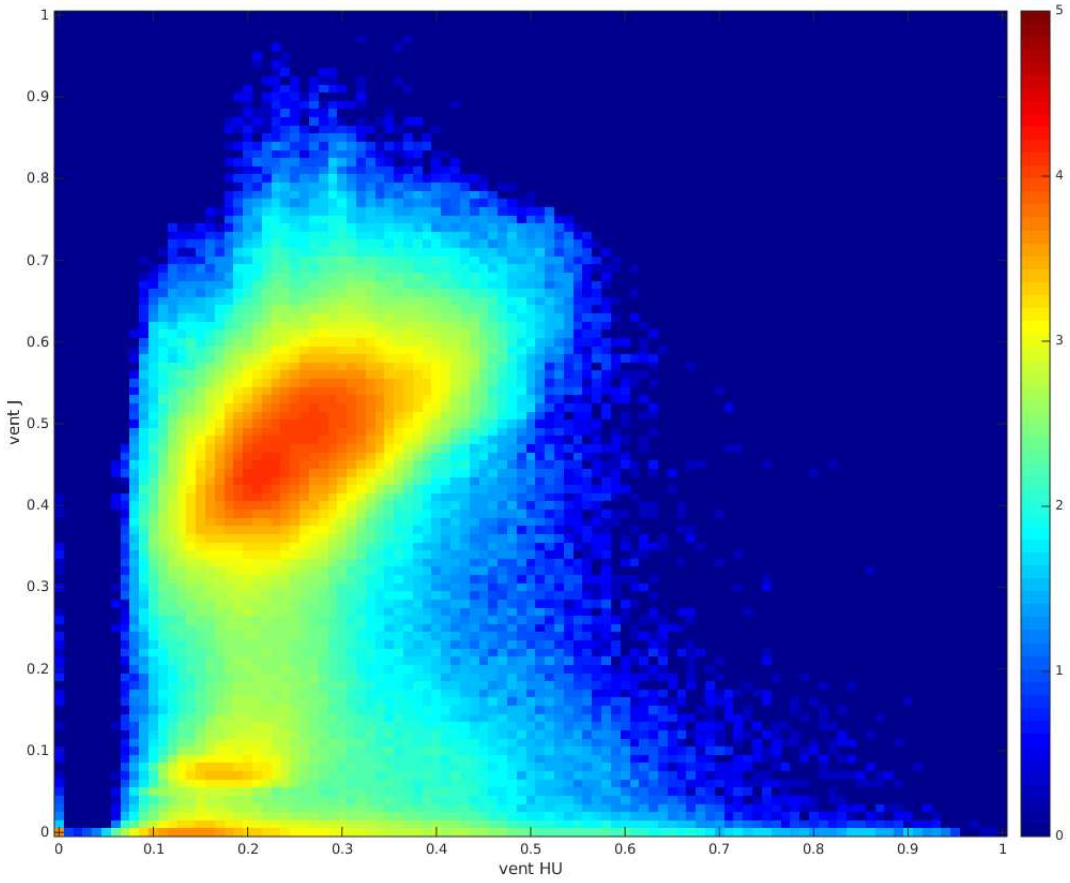

Figure 3. 2D histogram in log scale showing the relative distribution between HU derived and Jacobian based lung ventilation estimations.

To obtain voxelwise ventilation pattern, the probability density function of the Jacobian was computed through kernel density estimation method, where the Jacobian is considered a random variable. In our computation, the underlying probability density is assumed to be Gaussian distributed. Figure 4 shows examples of the characteristic voxel ventilation profiles in terms of their probability distribution of the Jacobian obtained through kernel

density estimation. To estimate the regional ventilation dynamically, Jacobian values corresponding to the cumulative probability percentiles are computed. Measures of volume change were computed by taking the ratio of the obtained Jacobian values and the 1%-ile Jacobian value. The lung ventilation maps at different ventilation maps are presented in a progression from low to high (Fig. 5).

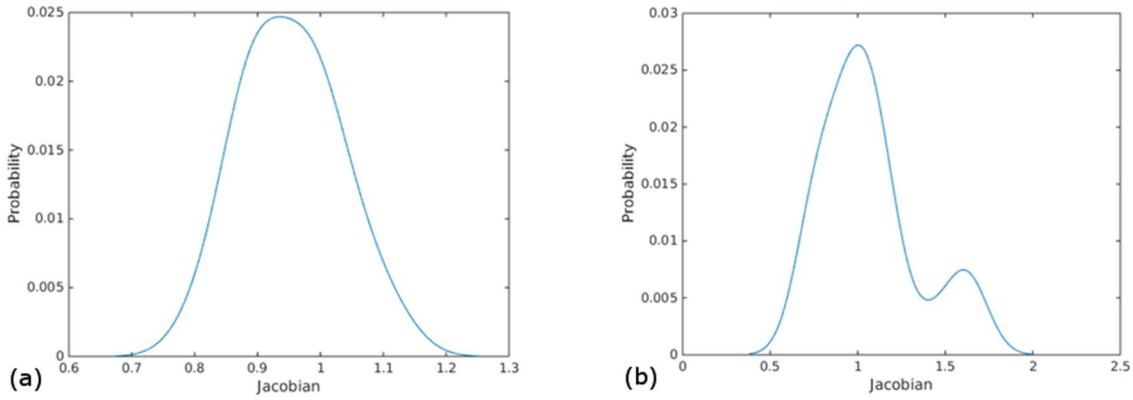

Figure 4. Examples of empirical probability distribution for two lung voxels as estimated from the 24 measured Jacobian values.

6.4 Discussion

Our proposed statistical Jacobian approach generates ventilation image is more robust than the conventional 4DCT ventilation images derived from Jacobian method in that a) our technique relies on rigorous statistical formulation that draws on volume change data from multiple samples instead of just the full exhalation and inhalation scans and b) 4DCT image data is prone to image artifact, while our fast helical CT data have temporal uncertainty of 0.12s which minimize any motion-induced uncertainty.

Our statistical Jacobian ventilation images show spatial heterogeneity, which correlates moderately well with the ventilation profile independently estimated using the voxel HU

directly. Good correlation between the two metrics was found in regions of high ventilation (Fig. 6), indicating good agreement between our proposed technique and conventional methodology based on specific volume. Deviation from the dominant trend was found mostly in the regime of low Jacobian values, where the HU based metric shows large variation. Such deviation is likely to be caused by mis-registration as well as cardiac motion induced motion uncertainties close to the heart-lung boundary.

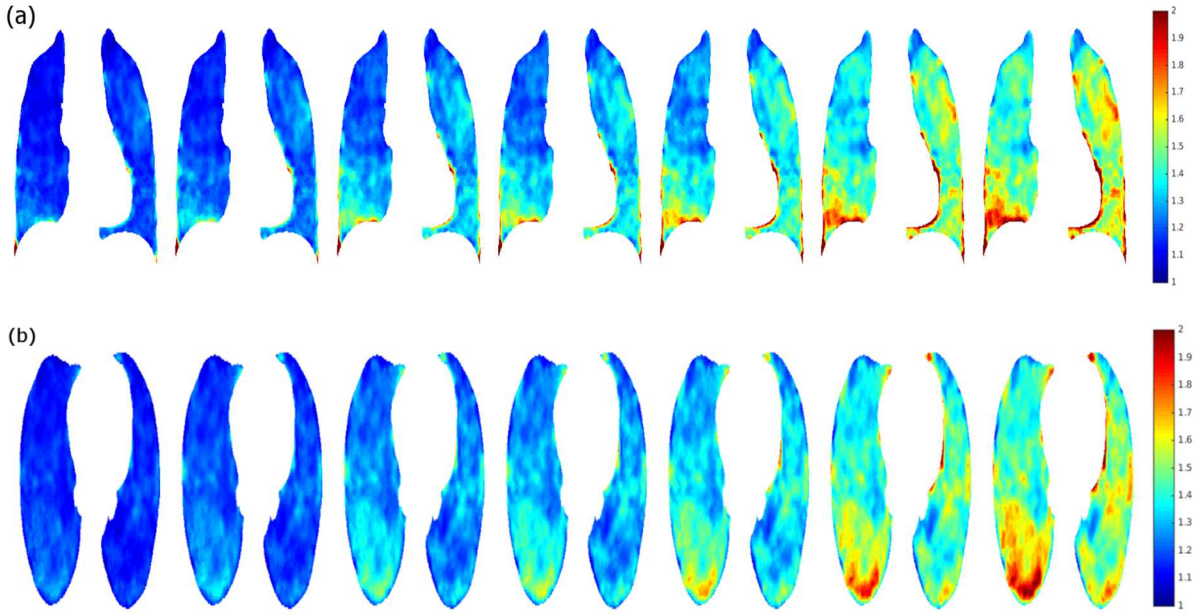

Figure 5. Quantitation of the dynamic ventilation levels of 20%-, 30%-, 50%-, 60%-, 75%-, 90%-, and 95%-ile from exhalation to inhalation (left to right). Colorbar gives the scale of the volume expansion.

Our dynamic ventilation estimation shows that the underlying ventilation pattern during quiet free breathing may not be normally distributed but can take on more complex distribution.

Our analysis shows a direct comparison between the two commonly adopted approaches using high quality fast helical CT image data that were processed using highly accurate

deformable registration algorithm. The comparison is presented in the entire lungs without potential bias that may be introduced through additional region selection for high ventilated region [120] or intensity thresholding [122, 130].

The highly heterogeneous ventilation distribution shows that assessing lung injury risks under the assumption of homogeneous lung function is susceptible to radiation risks. Since lung is a parallel organ, which is vulnerable to volume effect and late effect, accurate functional imaging provides the additional information to determine the optimal target coverage [125, 132, 133].

6.5 Conclusion

This work presented a novel technique for generating lung ventilation images using multiple Jacobian values computed through deformable image registration of the fast helical CT image data that are virtually free of motion artifacts. Assuming an identical and independent distribution which is unique to each lung voxel, the expectation values of the maximum and minimum Jacobian were computed. The difference between these two was computed and used as surrogate for voxel ventilation. The obtained Jacobian based ventilation metric was compared to the conventional HU based metric and good correlation was observed. Separately, voxel-wise ventilation distribution was computed by applying the kernel density estimation method on the sampled Jacobian values. The obtained ventilation probability function shows deviation to the normal distribution and the resulting ventilation map displays heterogeneity, indicating differences in regional function.

Chapter 7

Conclusion

7.1 Summary and Conclusions

The aims of this dissertation was to investigate the accuracy of a motion model, to develop a free-breathing lung density model, and to characterize the lung ventilation pattern, all using the high-pitch helically acquired lung CT data. Our motivation for the modeling works is not only limited to advancing the frontiers of imaging science but also to apply the gained knowledge to clinical scenarios where they may find the most diagnostic and therapeutic utility.

Current clinical 4DCT imaging commonly uses low-pitch helical CT protocol that performs axial scanning. In chapter 2, we employed the typical scanning parameters and conducted helical CT scanning experiments that simulate, at each couch position, the interplay between tumor under respiratory motion in the form of breathing traces and traveling CT couch. The simulated motion estimation was compared to the motion amplitude implied by the breathing trace. The frequencies of selected motion over- and under-estimation were compiled for a group of 50 patients. Our results show the scale of the problem in commercial 4DCT motion measurement.

In chapter 4, validation experiments were conducted that compare the motion model generated free-breathing images against the ground truth images of high-pitch helically acquired scans. Using an arbitrary reference image, our results showed the proposed 5DCT

technique can accurately reproduce the lung deformations associated with the variety of the sampled patient breathing states in the original free-breathing scans. In particular, it is robust in simulating the complex lung deformation involving large diaphragm displacements. Image similarity comparison showed that detailed lung anatomical features, such as nodules, bifurcations, and lung boundary, were very well aligned. The incorporation of a state-of-the-art deformable registration, deeds, preserves sliding motion on the lung boundary. Thus, the motion model can simulate such sliding motion and was made more general. The proposed ground truth based technique provided voxel-by-voxel accuracy analysis that could identify organ or tumor-specific motion modeling errors for treatment planning. Despite a large variety of breathing patterns and lung deformations, the 5DCT technique was able to accurately reproduce the original free-breathing helical CT scans, suggesting its wide applicability to lung cancer patients. Furthermore, such ground truth based analysis is unique in CT-based breathing motion modeling for radiation therapy and will provide uncertainty estimations in the model-based 4DCT breathing motion estimate of tumors and normal organs.

Chapter 5 investigated lung tissue densitometry through investigating a functional relationship that calibrates the density change of the human lung tissues under quiet free breathing conditions using unique fast helical CT data and deformable image registration. Accurate accounting of dynamic lung density variation is desirable and forms the basis for treatment planning calculations. This work applied mass conservation fitting between the tissue Hounsfield units and the Jacobian values and showed that there existed differential mechanical properties of the lung tissues, allowing for their classification into three broad types, namely, parenchyma (Type I), vasculature (Type II) and soft tissues (Type III). The

three types of tissues were separately modeled. The density modeling accuracy was assessed using large trials of leave-five-out cross validations, and the evaluated error was found to be comparable to the CT image noise. The proposed technique provided a valuable tool for performing human lung density analysis and will find important applications in pulmonary medical physics.

In chapter 6, lung functional mapping in the form of ventilation imaging was explored. Lung ventilation images have been generated based on the specific volume change or Jacobian mapping between the extremal phases in the 4DCT image set. Here we investigate a novel ventilation technique that is likewise motivated by the range of the regional volume changes as measured by the Jacobian metric. An algorithm was developed that computes the maximum and minimum Jacobian expectation value from the respective probability distribution function, which was constructed using the measured Jacobian values. Tissue specific ventilation was subsequently evaluated by taking the difference between these extremal values. The resulting ventilation map was compared with an independently generated map using the specific ventilation approach and good correlation was observed, especially in regions of high ventilation levels.

To assess the voxelwise ventilation distribution, a probability function was constructed from the set of Jacobian values using kernel density estimation. The percentile based ventilation image was then constructed from the specific volume expansion level. Such images represent the dynamic ventilation image.

7.2 Outlook

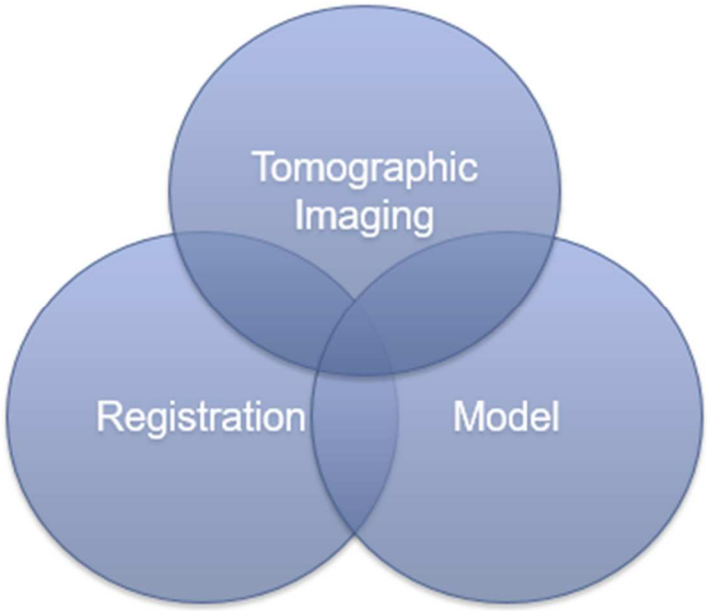

Figure 1. The essential elements that determine the simulation accuracy of the modeled physiological system.

In view of physiological model construction, the modeling framework may be represented as the intersection of three components, namely, the tomography imaging, the image registration, and the mathematical model. The tomographic imaging provides data samples of the organ under physiological motion; image registration measures the organ deformation; the modelling aims at characterizing the dynamic organ motion with a mathematical relationship. The improvement of any combination of the three components would make it possible to more accurately approximate the model performance of the dynamic system to the physical reality. This dissertation work presents the state-of-the-art tomographic imaging and image processing of the thoracic anatomy. The presented techniques for estimating lung tissue motion, density change, as well as ventilation imaging may not only find applications in different treatment modalities in radiation oncology but

also can become clinical tools that determine lung physiology and functionality in pulmonary medicine. We envision that the accuracy of our techniques will further improve with next generations of CT scanners that will have faster rotation time and couch speed as well as more accurate deformable algorithms for image processing in addition to other modeling approaches.

The accuracy level in the validation results for simulating the fast helical CT images with the lung motion model shows the great application potential of the model in CBCT imaging. Current clinical solution to on board CBCT imaging suffers in image quality due to limited projection sampling. A promising strategy to improve the CBCT imaging is to incorporate the motion model into the CBCT acquisition and reconstruction workflow such that the prior motion model parameters obtained through the patient planning session can be used to iteratively estimate the current model parameters and reference volume image simultaneously through minimizing the difference between the simulated and acquired projection images. If successful, the obtained treatment day CBCT images can be used for adaptive treatment planning that takes into account of the changes in the anatomy.

Lung densitometry and ventilation imaging based on fast helical CT imaging are novel techniques for assessing lung function. Monitoring the changes in density model parameters and regional ventilation level may be helpful to assess tissue damage following irradiation. Functional avoidance may be incorporated in the treatment planning process that preserves regions which undergo large gas exchange. In the near future, ventilation imaging should be employed in conjunction with perfusion imaging to further provide functional mapping to aid clinicians in their diagnosis.

Bibliography

1. American Cancer Society. Cancer Facts and Figures. 2015.

2. Machtay M, Bae K, Movsas B et al. Higher Biologically Effective Dose of Radiotherapy Is Associated with Improved Outcomes for Locally Advanced Non-Small Cell Lung Carcinoma Treated with Chemoradiation: An Analysis of the Radiation Therapy Oncology Group. *Int J Radiat Oncol* 2012; **82**: 425-34.

3. Timmerman R, Paulus R, Galvin J et al. Stereotactic Body Radiation Therapy for Inoperable Early Stage Lung Cancer. *Jama-J Am Med Assoc* 2010; **303**: 1070-6.

4. Stevens CW, Munden RF, Forster KM et al. Respiratory-driven lung tumor motion is independent of tumor size, tumor location, and pulmonary function. *Int J Radiat Oncol* 2001; **51**: 62-8.

5. Seppenwoolde Y, Shirato H, Kitamura K et al. Precise and real-time measurement of 3D tumor motion in lung due to breathing and heartbeat, measured during radiotherapy. *Int J Radiat Oncol* 2002; **53**: 822-34.

6. 4. Definition of Volumes. *Journal of the ICRU* 2010; **10**: 41-53.

7. Rietzel E, Liu AK, Chen GTY, Choi NC. Maximum-intensity volumes for fast contouring of lung tumors including respiratory motion in 4DCT planning. *Int J Radiat Oncol* 2008; **71**: 1245-52.

8. Rietzel E, Chen GTY, Choi NC, Willet CG. Four-dimensional image-based treatment planning: Target volume segmentation and dose calculation in the presence of respiratory motion. *Int J Radiat Oncol* 2005; **61**: 1535-50.

9. Bradley JD, Nofal AN, El Naqa IM et al. Comparison of helical, maximum intensity projection (MIP), and averaged intensity (Al) 4D CT imaging for stereotactic body radiation therapy (SBRT) planning in lung cancer. *Radiother Oncol* 2006; **81**: 264-8.

10. Underberg RWM, Lagerwaard FJ, Slotman BJ et al. Use of maximum intensity projections (MIP) for target volume generation in 4DCT scans for lung cancer. *Int J Radiat Oncol* 2005; **63**: 253-60.

11. St James S, Mishra P, Hacker F et al. Quantifying ITV instabilities arising from 4DCT: a simulation study using patient data. *Phys Med Biol* 2012; **57**: L1-L7.

12. Muirhead R, Mcnee SG, Featherstone C et al. Use of Maximum Intensity Projections (MIPs) for Target Outlining in 4DCT Radiotherapy Planning. *J Thorac Oncol* 2008; **3**: 1433-8.

13. Cai J, Read PW, Baisden JM et al. Estimation of error in maximal intensity projection-based internal target volume of lung tumors: A simulation and comparison study using dynamic magnetic resonance imaging. *Int J Radiat Oncol* 2007; **69**: 895-902.

14. Ge H, Cai J, Kelsey CR, Yin FF. Quantification and minimization of uncertainties of internal target volume for stereotactic body radiation therapy of lung cancer. *Int J Radiat Oncol Biol Phys* 2013; **85**: 438-43.

15. Wang ZH, Wu QJ, Marks LB et al. Cone-beam CT localization of internal target volumes for stereotactic body radiotherapy of lung lesions. *Int J Radiat Oncol* 2007; **69**: 1618-24.

16. Lamb JM, Robinson C, Bradley J et al. Generating lung tumor internal target volumes from 4D-PET maximum intensity projections. *Med Phys* 2011; **38**: 5732-7.

17. Van de Steene J, Van den Heuvel F, Bel A et al. Electronic portal imaging with on-line correction of setup error in thoracic irradiation: Clinical evaluation. *Int J Radiat Oncol* 1998; **40**: 967-76.

18. Coggle JE, Lambert BE, Moores SR. Radiation Effects in the Lung. *Environ Health Persp* 1986; **70**: 261-91.

19. Martel MK, Ten Haken RK, Hazuka MB et al. Dose-volume histogram and 3-D/CT treatment planning evaluation of patients with radiation pneumonitis. *International Journal of Radiation Oncology • Biology • Physics*; **24**: 173-4.

20. Emami B, Lyman J, Brown A et al. Tolerance of Normal Tissue to Therapeutic Irradiation. *Int J Radiat Oncol* 1991; **21**: 109-22.

21. Hanley J, Debois MM, Mah D et al. Deep inspiration breath-hold technique for lung tumors: The potential value of target immobilization and reduced lung density in dose escalation. *Int J Radiat Oncol* 1999; **45**: 603-11.

22. Mah D, Hanley J, Rosenzweig KE et al. Technical aspects of the deep inspiration breath-hold technique in the treatment of thoracic cancer. *Int J Radiat Oncol* 2000; **48**: 1175-85.

23. Rosenzweig KE, Hanley J, Mah D et al. The deep inspiration breath-hold technique in the treatment of inoperable non-small-cell lung cancer. *Int J Radiat Oncol* 2000; **48**: 81-7.

24. Barnes EIA, Murray BR, Robinson DM et al. Dosimetric evaluation of lung tumor immobilization using breath hold at deep inspiration. *Int J Radiat Oncol* 2001; **50**: 1091-8.

25. Ohara K, Okumura T, Akisada M et al. Irradiation Synchronized with Respiration Gate. *Int J Radiat Oncol* 1989; **17**: 853-7.

26. Inada T, Tsuji H, Hayakawa Y et al. [Proton irradiation synchronized with respiratory cycle]. *Nihon Igaku Hoshasen Gakkai Zasshi* 1992; **52**: 1161-7.

27. Kubo HD, Hill BC. Respiration gated radiotherapy treatment: A technical study. *Physics in Medicine and Biology* 1996; **41**: 83-91.

28. Kubo HD, Len PM, Minohara S, Mostafavi H. Breathing-synchronized radiotherapy program at the University of California Davis Cancer Center. *Medical Physics* 2000; **27**: 346-53.

29. Vedam SS, Kini VR, Keall PJ et al. Quantifying the predictability of diaphragm motion during respiration with a noninvasive external marker. *Med Phys* 2003; **30**: 505-13.

30. Wagman R, Yorke E, Ford E et al. Respiratory gating for liver tumors: use in dose escalation. *International Journal of Radiation Oncology* Biology* Physics* 2003; **55**: 659-68.

31. Gierga DP, Brewer J, Sharp GC et al. The correlation between internal and external markers for abdominal tumors: implications for respiratory gating (vol 61, pg 1551, 2005). *Int J Radiat Oncol* 2005; **62**: 1257-.

32. Berbeco RI, Nishioka S, Shirato H et al. Residual motion of lung tumours in gated radiotherapy with external respiratory surrogates. *Phys Med Biol* 2005; **50**: 3655-67.

33. Wu H, Zhao Q, Berbeco RI et al. Gating based on internal/external signals with dynamic correlation updates. *Phys Med Biol* 2008; **53**: 7137-50.

34. Cui Y, Dy JG, Sharp GC et al. Robust fluoroscopic respiratory gating for lung cancer radiotherapy without implanted fiducial markers. *Phys Med Biol* 2007; **52**: 741-55.

35. Berbeco RI, Mostafavi H, Sharp GC, Jiang SB. Towards fluoroscopic respiratory gating for lung tumours without radiopaque markers. *Phys Med Biol* 2005; **50**: 4481-90.

36. Cui Y, Dy JG, Alexander B, Jiang SB. Fluoroscopic gating without implanted fiducial markers for lung cancer radiotherapy based on support vector machines. *Phys Med Biol* 2008; **53**: N315-27.

37. Li R, Lewis JH, Cervino LI, Jiang SB. A feasibility study of markerless fluoroscopic gating for lung cancer radiotherapy using 4DCT templates. *Phys Med Biol* 2009; **54**: N489-500.

38. Cai J, McLawhorn R, Read PW et al. Effects of breathing variation on gating window internal target volume in respiratory gated radiation therapy. *Med Phys* 2010; **37**: 3927-34.

39. Keall PJ, Kini VR, Vedam SS, Mohan R. Motion adaptive x-ray therapy: a feasibility study. *Phys Med Biol* 2001; **46**: 1-10.

40. Ozhasoglu C, Saw CB, Chen HC et al. Synchrony - CyberKnife respiratory compensation technology. *Medical Dosimetry* 2008; **33**: 117-23.

41. Dempsey JF, Benoit D, Fitzsimmons JR et al. A device for realtime 3D image-guided IMRT. *Int J Radiat Oncol* 2005; **63**: S202-S.

42. Fallone B, Carlone M, Murray B et al. Development of a Linac-MRI system for real-time ART. *Med Phys* 2007; **34**: 2547-.

43. Lagendijk J, Raaymakers B, van der Heide U et al. In room magnetic resonance imaging guided radiotherapy (MRIgRT). *Med Phys* 2005; **32**: 2067-.

44. Vedam SS, Keall PJ, Kini VR et al. Acquiring a four-dimensional computed tomography dataset using an external respiratory signal. *Phys Med Biol* 2003; **48**: 45-62.

45. Ford EC, Mageras GS, Yorke E, Ling CC. Respiration-correlated spiral CT: A method of measuring respiratory-induced anatomic motion for radiation treatment planning. *Med Phys* 2003; **30**: 88-97.

46. Low DA, Nystrom M, Kalinin E et al. A method for the reconstruction of four-dimensional synchronized CT scans acquired during free breathing. *Med Phys* 2003; **30**: 1254-63.

47. McClelland JR, Blackall JM, Tarte S et al. A continuous 4D motion model from multiple respiratory cycles for use in lung radiotherapy. *Med Phys* 2006; **33**: 3348-58.

48. Zhang YB, Yang JZ, Zhang LF et al. Modeling respiratory motion for reducing motion artifacts in 4D CT images. *Med Phys* 2013; **40**.

49. Zhang QH, Pevsner A, Hertanto A et al. A patient-specific respiratory model of anatomical motion for radiation treatment planning. *Med Phys* 2007; **34**: 4772-81.

50. Low DA, Parikh PJ, Lu W et al. Novel breathing motion model for radiotherapy. *Int J Radiat Oncol* 2005; **63**: 921-9.

51. Zhao TY, Lu W, Yang DS et al. Characterization of free breathing patterns with 5D lung motion model. *Med Phys* 2009; **36**: 5183-9.

52. Marks LB, Spencer DP, Sherouse GW et al. The role of three dimensional functional lung imaging in radiation treatment planning: the functional dose-volume histogram. *Int J Radiat Oncol Biol Phys* 1995; **33**: 65-75.

53. Harris RS, Schuster DP. Visualizing lung function with positron emission tomography. *J Appl Physiol* 2007; **102**: 448-58.

54. Moller HE, Chen XJ, Saam B et al. MRI of the lungs using hyperpolarized noble gases. *Magn Reson Med* 2002; **47**: 1029-51.

55. van Beek EJR, Wild JM, Kauczor HU et al. Functional MRI of the lung using hyperpolarized 3-helium gas. *J Magn Reson Imaging* 2004; **20**: 540-54.

56. Hoffman EA, van Beek E. Hyperpolarized media MR imaging - Expanding the boundaries? *Acad Radiol* 2006; **13**: 929-31.

57. Chon D, Simon BA, Beck KC et al. Differences in regional wash-in and wash-out time constants for xenon-CT ventilation studies. *Resp Physiol Neurobi* 2005; **148**: 65-83.

58. Guerrero T, Sanders K, Noyola-Martinez J et al. Quantification of regional ventilation from treatment planning CT. *Int J Radiat Oncol* 2005; **62**: 630-4.

59. Liu HH, Balter P, Tutt T et al. Assessing respiration-induced tumor motion and internal target volume using four-dimensional computed tomography for radiotherapy of lung cancer. *Int J Radiat Oncol* 2007; **68**: 531-40.

60. Donnelly ED, Parikh PJ, Lu W et al. Assessment of intrafraction mediastinal and hilar lymph node movement and comparison to lung tumor motion using four-dimensional CT. *Int J Radiat Oncol* 2007; **69**: 580-8.

61. Keall PJ, Starkschall G, Shukla H et al. Acquiring 4D thoracic CT scans using a multislice helical method. *Phys Med Biol* 2004; **49**: 2053-67.

62. Pan T, Lee TY, Rietzel E, Chen GTY. 4D-CT imaging of a volume influenced by respiratory motion on multi-slice CT. *Medical Physics* 2004; **31**: 333-40.

63. Lu W, Low DA, Parikh PJ et al. Comparison of spirometry and abdominal height as four-dimensional computed tomography metrics in lung. *Medical Physics* 2005; **32**: 2351-7.

64. Lu W, Parikh PJ, Hubenschmidt JP et al. A comparison between amplitude sorting and phase-angle sorting using external respiratory measurement for 4D CT. *Med Phys* 2006; **33**: 2964-74.

65. Guckenberger M, Weininger M, Wilbert J et al. Influence of retrospective sorting on image quality in respiratory correlated computed tomography. *Radiother Oncol* 2007; **85**: 223-31.

66. Abdelnour AF, Nehmeh SA, Pan T et al. Phase and amplitude binning for 4D-CT imaging. *Phys Med Biol* 2007; **52**: 3515-29.

67. Fitzpatrick MJ, Starkschall G, Antolak JA et al. Displacement-based binning of time-dependent computed tomography image data sets. *Medical Physics* 2006; **33**: 235-46.

68. Rietzel E, Pan TS, Chen GTY. Four-dimensional computed tomography: Image formation and clinical protocol. *Med Phys* 2005; **32**: 874-89.

69. Yamamoto T, Langner U, Loo Jr BW et al. Retrospective Analysis of Artifacts in Four-Dimensional CT Images of 50 Abdominal and Thoracic Radiotherapy Patients. *International Journal of Radiation Oncology*Biology*Physics* 2008; **72**: 1250-8.

70. Cai J, McLawhorn R, Read PW et al. Effects of breathing variation on gating window internal target volume in respiratory gated radiation therapya). *Medical Physics* 2010; **37**: 3927-34.

71. Sarker J, Chu A, Mui K et al. Variations in tumor size and position due to irregular breathing in 4D-CT: A simulation study. *Medical Physics* 2010; **37**: 1254-60.

72. Ehrhardt J, Werner R, Saring D et al. An optical flow based method for improved reconstruction of 4D CT data sets acquired during free breathing. *Med Phys* 2007; **34**: 711-21.

73. Hertanto A, Zhang QH, Hu YC et al. Reduction of irregular breathing artifacts in respiration-correlated CT images using a respiratory motion model. *Med Phys* 2012; **39**: 3070-9.

74. Langner UW, Keall PJ. Accuracy in the localization of thoracic and abdominal tumors using respiratory displacement, velocity, and phase. *Medical Physics* 2009; **36**: 386-93.

75. Thomas D, Lamb J, White B et al. A Novel Fast Helical 4D-CT Acquisition Technique to Generate Low-Noise Sorting Artifact–Free Images at User-Selected Breathing Phases. *International journal of radiation oncology, biology, physics* 2014; **89**: 191-8.

76. Werner R, White B, Handels H et al. Technical Note: Development of a tidal volume surrogate that replaces spirometry for physiological breathing monitoring in 4D CT. *Medical Physics* 2010; **37**: 615-9.

77. Boldea V, Sharp GC, Jiang SB, Sarrut D. 4D-CT lung motion estimation with deformable registration: Quantification of motion nonlinearity and hysteresis. *Medical Physics* 2008; **35**: 1008-18.

78. Sarrut D, Boldea V, Miguet S, Ginestet C. Simulation of four-dimensional CT images from deformable registration between inhale and exhale breath-hold CT scans. *Medical Physics* 2006; **33**: 605-17.

79. Schreibmann E, Chen GTY, Xing L. Image interpolation in 4D CT using a BSpline deformable registration model. *Int J Radiat Oncol* 2006; **64**: 1537-50.

80. Kadoya N, Fujita Y, Katsuta Y et al. Evaluation of various deformable image registration algorithms for thoracic images. *J Radiat Res* 2014; **55**: 175-82.

81. Kashani R, Hub M, Balter JM et al. Objective assessment of deformable image registration in radiotherapy: A multi-institution study. *Med Phys* 2008; **35**: 5944-53.

82. Dou TH, Min Y, Neylon J et al. Fast simulated annealing and adaptive Monte Carlo sampling based parameter optimization for dense optical-flow deformable image registration of 4DCT lung anatomy. 2016; 2016. p. 97860N-N-18.

83. Murphy K, van Ginneken B, Reinhardt JM et al. Evaluation of Registration Methods on Thoracic CT: The EMPIRE10 Challenge. *Ieee T Med Imaging* 2011; **30**: 1901-20.

84. Heinrich MP, Jenkinson M, Bhushan M et al. MIND: Modality independent neighbourhood descriptor for multi-modal deformable registration. *Medical Image Analysis* 2012; **16**: 1423-35.

85. Heinrich MP, Jenkinson M, Brady M, Schnabel JA. MRF-Based Deformable Registration and Ventilation Estimation of Lung CT. *Ieee T Med Imaging* 2013; **32**: 1239-48.

86. Heinrich M, Jenkinson M, Papież B et al. Towards Realtime Multimodal Fusion for Image-Guided Interventions Using Self-similarities. In: Mori K, Sakuma I, Sato Y et al., eds. *Medical Image Computing and Computer-Assisted Intervention – MICCAI 2013*: Springer Berlin Heidelberg 2013:187-94.

87. Heinrich M, Jenkinson M, Brady S, Schnabel J. Globally Optimal Deformable Registration on a Minimum Spanning Tree Using Dense Displacement Sampling. In: Ayache N, Delingette H, Golland P, Mori K, eds. *Medical Image Computing and Computer-Assisted Intervention – MICCAI 2012*: Springer Berlin Heidelberg 2012:115-22.

88. Lassen B, Kuhnigk J-M, Schmidt M et al. Lung and lung lobe segmentation methods at Fraunhofer MEVIS. 4th Int MICCAI Workshop Pulmonary Image Anal, Toronto, Canada; 2011; 2011.

89. Bortfeld T, Jiang SB, Rietzel E. Effects of motion on the total dose distribution. *Seminars in Radiation Oncology* 2004; **14**: 41-51.

90. Keall PJ, Mageras GS, Balter JM et al. The management of respiratory motion in radiation oncology report of AAPM Task Group 76. *Med Phys* 2006; **33**: 3874-900.

91. Mutaf YD, Brinkmann DH. Optimization of internal margin to account for dosimetric effects of respiratory motion. *Int J Radiat Oncol* 2008; **70**: 1561-70.

92. Keall P. 4-dimensional computed tomography imaging and treatment planning. *Semin Radiat Oncol* 2004; **14**: 81-90.

93. Admiraal MA, Schuring D, Hurkmans CW. Dose calculations accounting for breathing motion in stereotactic lung radiotherapy based on 4D-CT and the internal target volume. *Radiotherapy and Oncology* 2008; **86**: 55-60.

94. Underberg RWM, Lagerwaard FJ, Slotman BJ et al. Benefit of respiration-gated stereotactic radiotherapy for stage I lung cancer: An analysis of 4DCT datasets. *Int J Radiat Oncol* 2005; **62**: 554-60.

95. Nelson C, Starkschall G, Chang JY. The potential for dose escalation in lung cancer as a result of systematically reducing margins used to generate planning target volume. *Int J Radiat Oncol* 2006; **65**: 573-86.

96. Benedict SH, Yenice KM, Followill D et al. Stereotactic body radiation therapy: The report of AAPM Task Group 101. *Med Phys* 2010; **37**: 4078-101.

97. Yamamoto T, Langner U, Loo BW et al. Retrospective Analysis of Artifacts in Four-Dimensional Ct Images of 50 Abdominal and Thoracic Radiotherapy Patients. *Int J Radiat Oncol* 2008; **72**: 1250-8.

98. Jiang SB. Radiotherapy of mobile tumors. *Semin Radiat Oncol* 2006; **16**: 239-48.

99. Johnston E, Diehn M, Murphy JD et al. Reducing 4D CT artifacts using optimized sorting based on anatomic similarity. *Med Phys* 2011; **38**: 2424-9.

100. Werner R, Ehrhardt J, Frenzel T et al. Motion Artifact Reducing Reconstruction of 4D CT Image Data for the Analysis of Respiratory Dynamics. *Methods of Information in Medicine* 2007; **46**: 254-60.

101. Zeng RP, Fessler JA, Balter JM, Balter PA. Iterative sorting for 4DCT images based on internal anatomy motion. *2007 4th Ieee International Symposium on Biomedical Imaging : Macro to Nano, Vols 1-3* 2007: 744-7.

102. Chi YW, Liang J, Qin X, Yan D. Respiratory motion sampling in 4DCT reconstruction for radiotherapy. *Med Phys* 2012; **39**: 1696-703.

103. Thomas D, Lamb J, White B et al. A Novel Fast Helical 4D-CT Acquisition Technique to Generate Low-Noise Sorting Artifact-Free Images at User-Selected Breathing Phases. *Int J Radiat Oncol* 2014; **89**: 191-8.

104. Low DA, White BM, Lee PP et al. A novel CT acquisition and analysis technique for breathing motion modeling. *Phys Med Biol* 2013; **58**: L31-L6.

105. Chen ML, Lu WG, Chen Q et al. A simple fixed-point approach to invert a deformation field. *Med Phys* 2008; **35**: 81-8.

106. Hurkmans CW, van Lieshout M, Schuring D et al. Quality Assurance of 4d-Ct Scan Techniques in Multicenter Phase Iii Trial of Surgery Versus Stereotactic Radiotherapy (Radiosurgery or Surgery for Operable Early Stage (Stage 1a) Non-Small-Cell Lung Cancer [Rosel] Study). *Int J Radiat Oncol* 2011; **80**: 918-27.

107. Knopf A, Bert C, Heath E et al. Special report: Workshop on 4D-treatment planning in actively scanned particle therapy—Recommendations, technical challenges, and future research directions. *Medical Physics* 2010; **37**: 4608-14.

108. Aarup LR, Nahum AE, Zacharatou C et al. The effect of different lung densities on the accuracy of various radiotherapy dose calculation methods: Implications for tumour coverage. *Radiotherapy and Oncology* 2009; **91**: 405-14.

109. McGurk R, Seco J, Riboldi M et al. Extension of the NCAT phantom for the investigation of intra-fraction respiratory motion in IMRT using 4D Monte Carlo. *Physics in Medicine and Biology* 2010; **55**: 1475-90.

110. Williams CL, Mishra P, Seco J et al. A mass-conserving 4D XCAT phantom for dose calculation and accumulation. *Medical Physics* 2013; **40**.

111. Heinrich MP, Jenkinson M, Papież BW et al. Towards realtime multimodal fusion for image-guided interventions using self-similarities. *Medical Image Computing and Computer-Assisted Intervention–MICCAI 2013*: Springer 2013:187-94.

112. Lassen B, Kuhnigk J-M, Schmidt M et al. Lung and lung lobe segmentation methods at Fraunhofer MEVIS. *4th Int MICCAI Workshop Pulmonary Image Anal, Toronto, Canada* 2011.

113. Rosenblum LJ, Mauceri RA, Wellenstein DE et al. Density Patterns in the Normal Lung as Determined by Computed-Tomography. *Radiology* 1980; **137**: 409-16.

114. Rey D, Subsol G, Delingette H, Ayache N. Automatic detection and segmentation of evolving processes in 3D medical images: Application to multiple sclerosis. *Med Image Anal* 2002; **6**: 163-79.

115. Townsley MI. Structure and composition of pulmonary arteries, capillaries, and veins. *Comprehensive Physiology* 2012.

116. Engelsman M, Rietzel E, Kooy HM. Four-dimensional proton treatment planning for lung tumors. *Int J Radiat Oncol* 2006; **64**: 1589-95.

117. Dou TH, Thomas DH, O'Connell DP et al. A Method for Assessing Ground-Truth Accuracy of the 5DCT Technique. *International Journal of Radiation Oncology*Biology*Physics* 2015; **93**: 925-33.

118. McShan DL, Kessler ML, Vineberg K, Fraass BA. Inverse plan optimization accounting for random geometric uncertainties with a multiple instance geometry approximation (MIGA). *Medical Physics* 2006; **33**: 1510-21.

119. Trofimov A, Rietzel E, Lu HM et al. Temporo-spatial IMRT optimization: concepts, implementation and initial results. *Physics in Medicine and Biology* 2005; **50**: 2779-98.

120. Castillo R, Castillo E, Martinez J, Guerrero T. Ventilation from four-dimensional computed tomography: density versus Jacobian methods. *Phys Med Biol* 2010; **55**: 4661-85.

121. Reinhardt JM, Ding K, Cao K et al. Registration-based estimates of local lung tissue expansion compared to xenon CT measures of specific ventilation. *Med Image Anal* 2008; **12**: 752-63.

122. Yamamoto T, Kabus S, Klinder T et al. Investigation of four-dimensional computed tomography-based pulmonary ventilation imaging in patients with emphysematous lung regions. *Phys Med Biol* 2011; **56**: 2279-98.

123. Ding K, Cao KL, Fuld MK et al. Comparison of image registration based measures of regional lung ventilation from dynamic spiral CT with Xe-CT. *Med Phys* 2012; **39**: 5084-98.

124. Brennan D, Schubert L, Diot Q et al. Clinical Validation of 4-Dimensional Computed Tomography Ventilation With Pulmonary Function Test Data. *Int J Radiat Oncol* 2015; **92**: 423-9.

125. Yamamoto T, Kabus S, von Berg J et al. Impact of Four-Dimensional Computed Tomography Pulmonary Ventilation Imaging-Based Functional Avoidance for Lung Cancer Radiotherapy. *Int J Radiat Oncol* 2011; **79**: 279-88.

126. Yaremko BP, Guerrero TM, Noyola-Martinez J et al. Reduction of normal lung irradiation in locally advanced non-small-cell lung cancer patients, using ventilation images for functional avoidance. *Int J Radiat Oncol* 2007; **68**: 562-71.

127. King MT, Maxim PG, Diehn M et al. Analysis of Long-Term 4-Dimensional Computed Tomography Regional Ventilation After Radiation Therapy. *Int J Radiat Oncol* 2015; **92**: 683-90.

128. Yamamoto T, Kabus S, Lorenz C et al. Pulmonary Ventilation Imaging Based on 4-Dimensional Computed Tomography: Comparison With Pulmonary Function Tests and SPECT Ventilation Images. *Int J Radiat Oncol* 2014; **90**: 414-22.

129. Yamamoto T, Kabus S, Lorenz C et al. 4D CT lung ventilation images are affected by the 4D CT sorting method. *Med Phys* 2013; **40**.

130. Guerrero T, Sanders K, Castillo E et al. Dynamic ventilation imaging from four-dimensional computed tomography. *Phys Med Biol* 2006; **51**: 777-91.

131. Du KF, Bayouth JE, Ding K et al. Reproducibility of intensity-based estimates of lung ventilation. *Med Phys* 2013; **40**.

132. Vinogradskiy Y, Castillo R, Castillo E et al. Use of 4-Dimensional Computed Tomography-Based Ventilation Imaging to Correlate Lung Dose and Function With Clinical Outcomes. *Int J Radiat Oncol* 2013; **86**: 366-71.

133. Yamamoto T, Kabus S, Bal M et al. The first patient treatment of computed tomography ventilation functional image-guided radiotherapy for lung cancer. *Radiotherapy and Oncology* 2016; **118**: 227-31.